Project 2:
LDV Measurement and Flow Visualization of a Cone in a Low Speed Water Tunnel

AAE 520 - Experimental Aerodynamics

Instructor: Steven P. Schneider
Teaching Assistant: Mark Wason

Authors:
Javier Cortina Fernández
Alberto Marín Cebrián

February 19^{th}, 2018

Contents

List of Figures

Nomenclature

Magnitudes

α	Angle of attack
Δ	Uncertainty of a quantity
δ	Increment
λ	Wavelength
$\mathbb{P}$	Probability
μ	Dynamic viscosity of the fluid
$\overline{U}$	Mean velocity of the flow
ρ	Density of the fluid
σ	Standard deviation
σ^2	Variance
θ	Angle between the crossed beams
ξ	Scale parameter (Weibull distribution)
a, b, c	Sides of the triangle formed to measure θ
F	General function
f	Frequency
k	Shape parameter (Weibull distribution)
l_c	Characteristic length of a body
N	Number of samples taken in a set of data
Re	Reynolds number
T	Temperature
U	Flow velocity
U'	Velocity fluctuation of the flow
x	Coordinate in the downstream location

Subscripts

∞	Free stream quantity
i	i^{th} element of a set of data.
N	Normal distribution.
rms	Root mean square.
W	Weibull distribution.

1 Abstract

This experiment was divided into two different sets of experiments, LDV measurements and flow visualization. Differences between flowmeter and LDV velocities were studied, and the velocity distribution of the particles in the free stream was compared with the Weibull and normal distribution functions. Also, the root mean square velocity and turbulence of the free stream were studied. From the flow visualization perspective, the flow around a cone was studied at different velocities and angles of attack.

2 Introduction

In fluid dynamics there are some situations where there is no simple analytical solution to predict the flow, so experimental techniques must be employed. One of this situations is the subsonic flow around a cone at a high angles of attack. Studying how the flow behaves in these conditions has many applications, such as the nose of fighter jets when maneuvering at high angles of attack. In order to study the subsonic flow at high angles of attack, a water tunnel was used. The main motivation behind using a water tunnel for this lab is that it enables easy flow visualization with dye, and has large enough particles to measure velocities with a Laser Doppler Velocimeter. Flow visualization can give an insight into the complex flow behaviour around models, enabling researchers to obtain an understanding of the fluid dynamics of the flow. An example of previous work using a water tunnel to visualize the flow is displayed in Fig. (1).

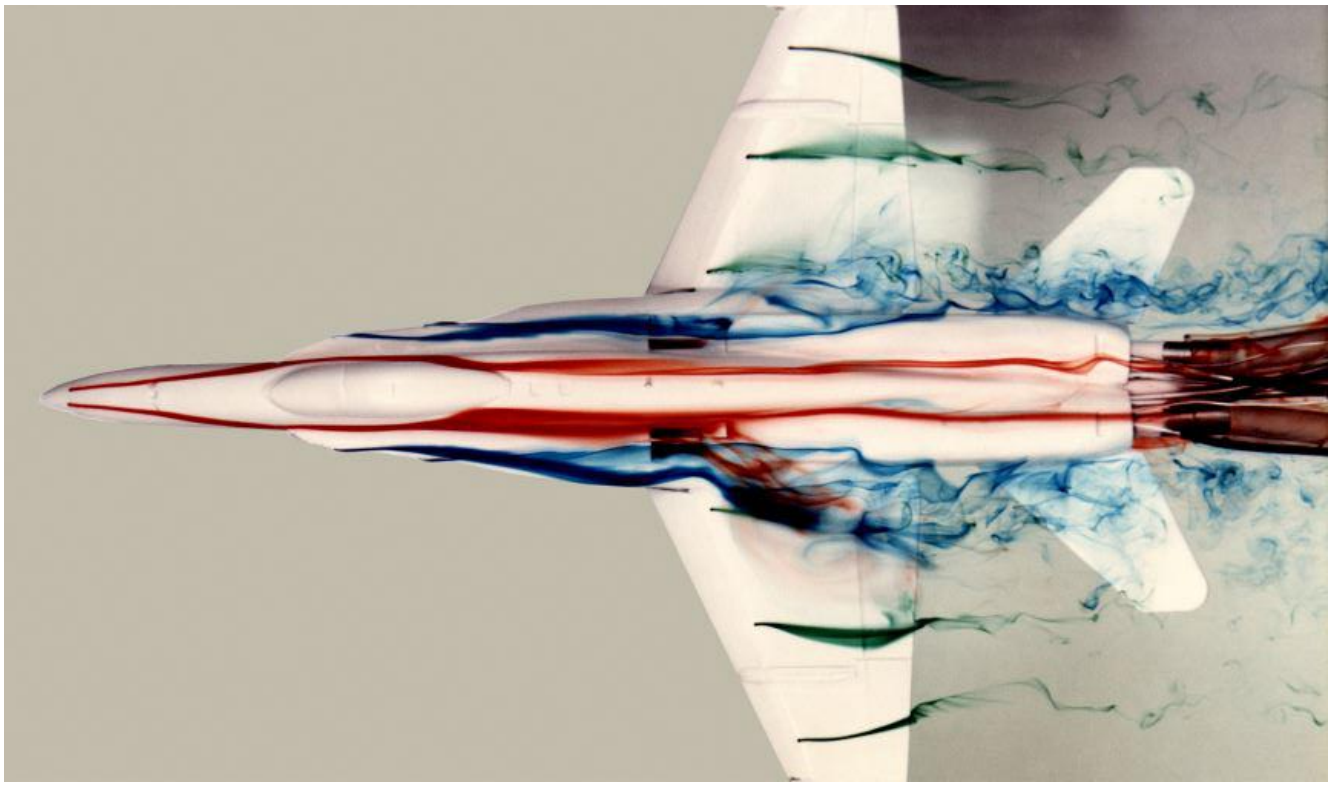

Figure 1: F-18 water tunnel tests in Flow Visualization Facility NASA/Dryden (Source: [1]).

2.1 Objectives

The objectives of the experiments were to:

- Gather precise velocity data using LDV.
- Correlate flow meter readings to absolute velocities given by the LDV and identify the major sources of error.
- Study the velocity distribution of particles in the free stream.
- Use dye to visualize the flow around a cone and identify different flow regimes.
- Identify sources of error and propose possible solutions for them.

3 Background

3.1 Laboratory instruments

3.1.1 Low speed water tunnel

Wind tunnels are very useful tools used to recreate fluid flows past solid objects in a controlled manner. Such objects, often called a wind tunnel models, can be instrumented with suitable sensors in order to measure aerodynamic forces, pressure distribution, or other aerodynamic-related characteristics. Another interesting approach is to use water instead of air in the tunnel. In the past, water tunnels have primarily been used to carry out detailed flow visualization studies using scaled models, such as aircraft [2]. They are better suited to flow visualization studies than are wind tunnels, due to water having a higher density and lower mass diffusivity than air, and the fact that the free-stream velocities used in water tunnels are generally substantially less than those used in wind tunnels.

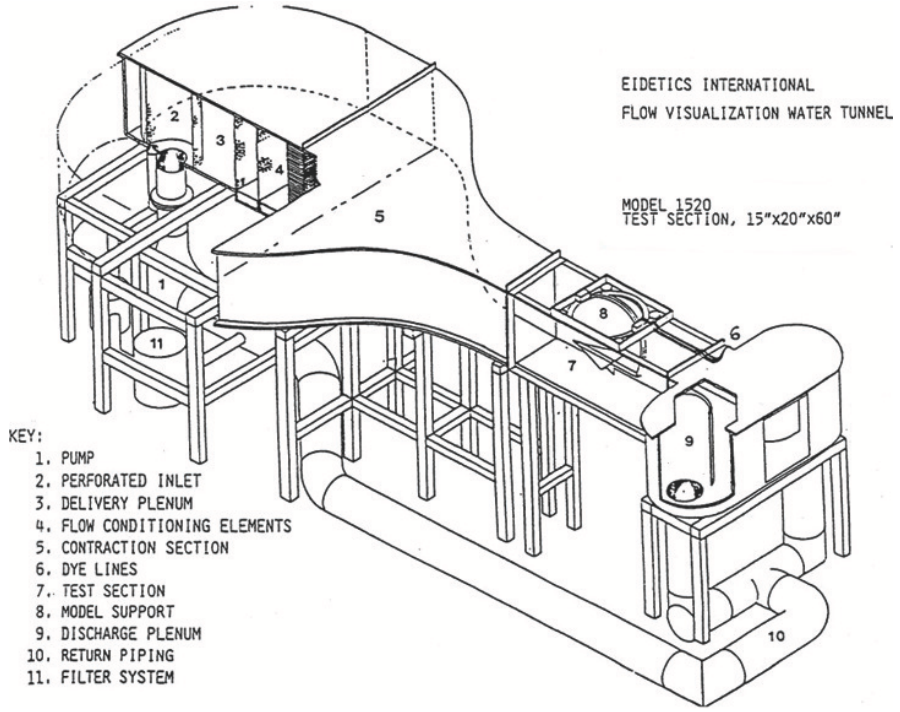

Figure 2: Water tunnel used in the laboratory.

The water tunnel used in the laboratory is displayed in Fig. (2). It is a closed-loop tunnel, which operates as a continuous flow channel pumping 1000 gallons of water at a variable speeds up to 12 in/s using a 15 Hp, 3-phase motor. Also, the tunnel is equipped with a flowmeter to measure the velocity of the flow inside the test section. The test section has clear plexiglass walls on both sides in order to better observe the flow, and measure the absolute velocity with the LDV. Lastly, it has a dye supply system used to visualize the flow around the tunnel models.

3.1.2 Laser Doppler Velocimeter

In order to precisely measure the absolute velocity of the water, Laser Doppler Velocimetry (LDV) was used. LDV is the technique of using the Doppler shift in a laser beam to measure the velocity in transparent or semi-transparent fluid flows. In this experiment, the LDV was used to measure the velocity of the particles flowing in the tunnel. It was found that regular unfiltered tap water had enough particles for the LDV to work correctly. Further explanations of the physics behind this measuring device are included in Section (3.3). Also, a sketch of the LDV used in the experiment is displayed in Fig. (3), and pictures of the actual LDV are displayed in Fig. (4).

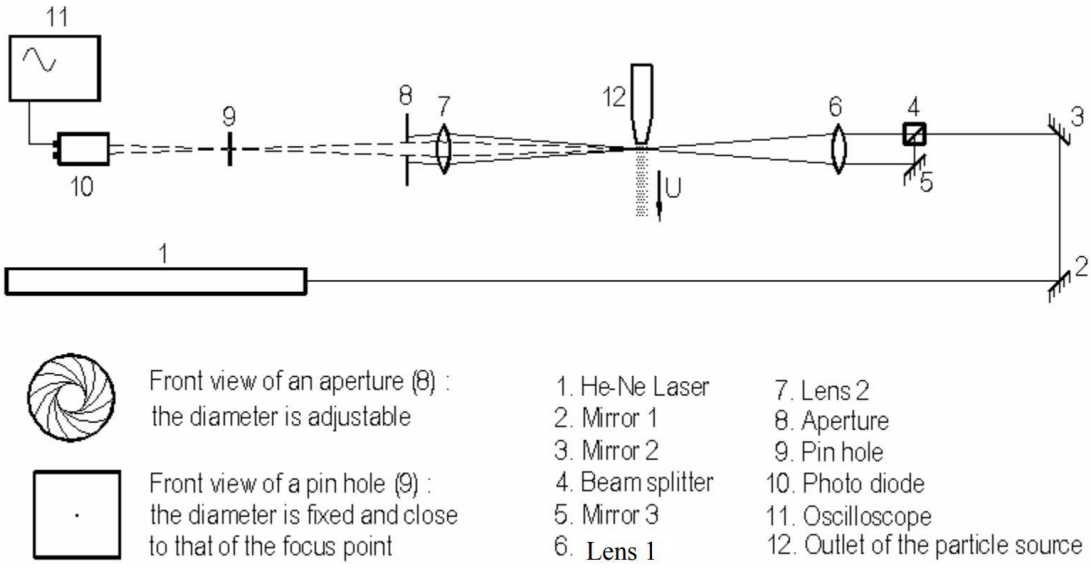

Figure 3: Sketch of the LDV setup used in the experiment.

The LDV was mounted on a support system that enabled the precise translation of the LDV setup in the three different axes by means of hand-cranks. Thus, the point of intersection between the beams could be precisely moved to measure the velocity at different locations inside the tunnel.

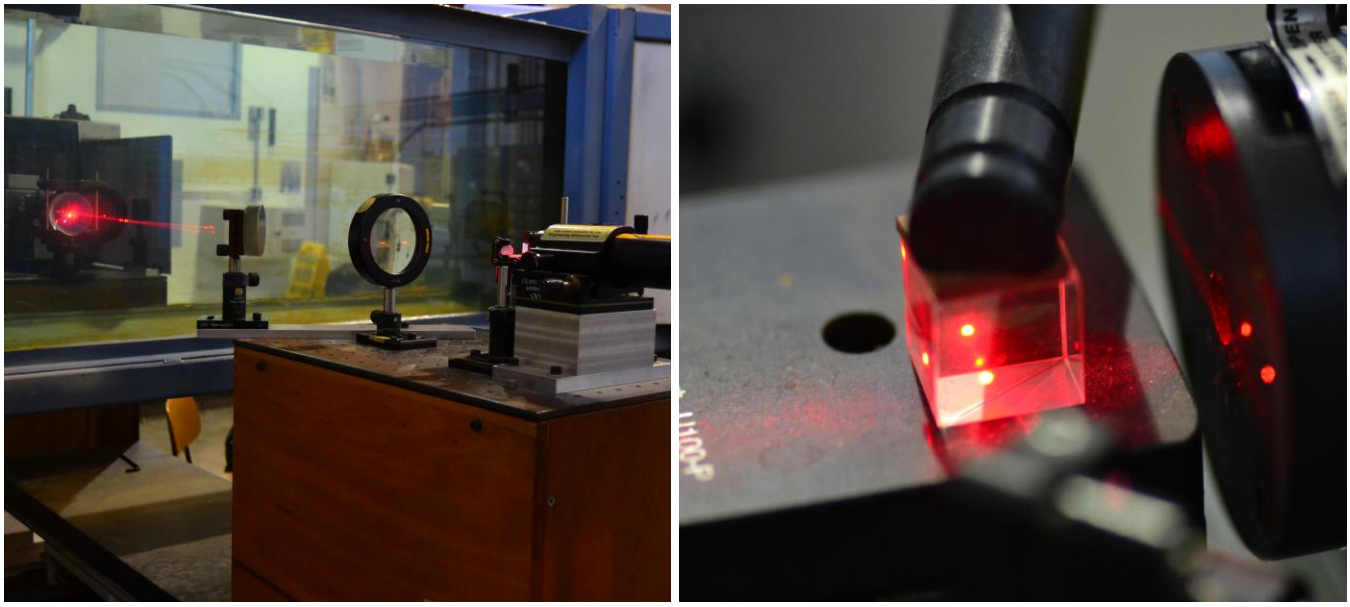

(a) LDV setup crossing the tunnel.

(b) Closeup of the beam splitter.

Figure 4: LDV setup used in the experiment.

3.1.3 Oscilloscope

An oscilloscope is an instrument capable of measuring a wide variety of rapidly changing electrical phenomena. The oscilloscope graphs the changes in voltage on its vertical axis, and its elapsed time on the horizontal axis. It can also calculate the average value of an unsteady voltage signal, and export the waveform of the signal received over a period of time.

Figure 5: Oscilloscope used in the experiment (Courtesy of *Tektronix*).

All of those characteristics make it a great instrument for measuring the voltage variations given by the photomultiplier. The photomultiplier is the photo diode of the LDV that emits an output signal proportional to the intensity of the captured light when a single particle traverses the measuring volume [3].

3.1.4 Test object

The test object that was analyzed in the water tunnel was a forebody cone that could be adjusted at an angle of attack of up to $\alpha = 20^o$. The angle of attack was measured with a digital magnetic angle gauge level, that had a precision of $\Delta\alpha = 0.1^o$. A sketch of the forebody cone used in the experiment is displayed in Fig. (6). Measurements in Fig. (6) are accurate up to a thousandth of an inch, thus, the error in these measurements was considered to be of $\pm 0.001\ in$.

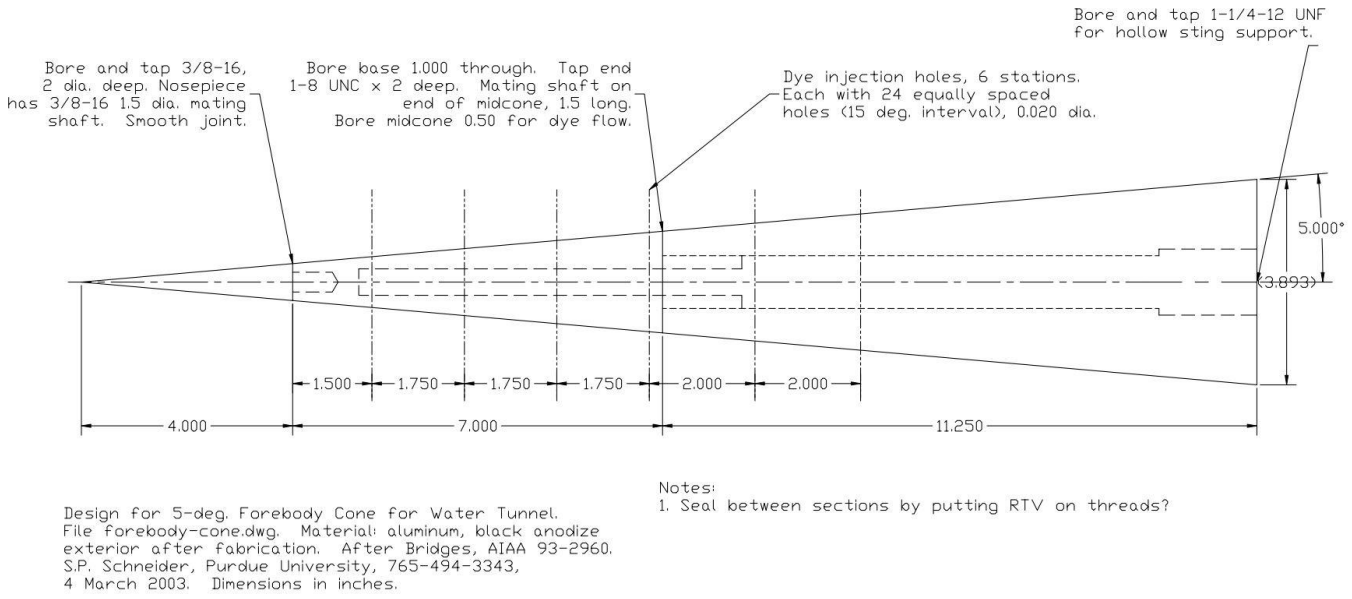

Figure 6: Sketch of the forebody cone used in the experiment.

Furthermore, as it can be observed in Fig. (6), the cone had dye injection holes that enabled the flow visualization. The flow visualization photos were captured with a Nikon D3100 reflex camera with an attached Nikon AF-S VR Micro-NIKKOR 105mm f/2.8G IF-ED Lens.

3.2 Error propagation

Error is an inherent property of measurements. Measuring devices interact with their environment perturbing the physical quantity they measure. Also, some errors may appear given by the limited precision of such measuring devices. Although these inaccuracies are typically small, it is important to take them into account when using experimental data to make calculations. How errors of different variables propagate in further calculations must be considered. The effect of these errors on the uncertainty of a function is calculated using Eq. (1):

$$\Delta F(x, y, z, ...) = \sqrt{\left[\left(\frac{\partial F}{\partial x}\right)\Delta x\right]^2 + \left[\left(\frac{\partial F}{\partial y}\right)\Delta y\right]^2 + \left[\left(\frac{\partial F}{\partial z}\right)\Delta z\right]^2 + \ ...} \tag{1}$$

where F is the function and x, y and z are its variables with given errors.

The initial uncertainties of the different variables measured, and how these values affect the final results are discussed throughout the report.

3.3 Laser Doppler Velocimetry

The LDV crosses two beams of collimated, monochromatic and coherent laser light in the flow field of interest. The two beams are obtained by splitting a single beam in order to ensure good coherence, as depicted in Figs. (3) and (4b). According to the Doppler effect, the change in frequency of the reflected radiation is a function of the targeted object's relative velocity, which in this case refers to a particular particle in the fluid. Particles moving through the fringes scatter light whose intensity fluctuates with a frequency that is related to the particle's velocity. Thus, the velocity of the particle can be obtained by measuring the change in frequency of the reflected laser light. This is done by forming an interference fringe pattern referred to as the Young's interference fringes, as shown in Fig. (7).

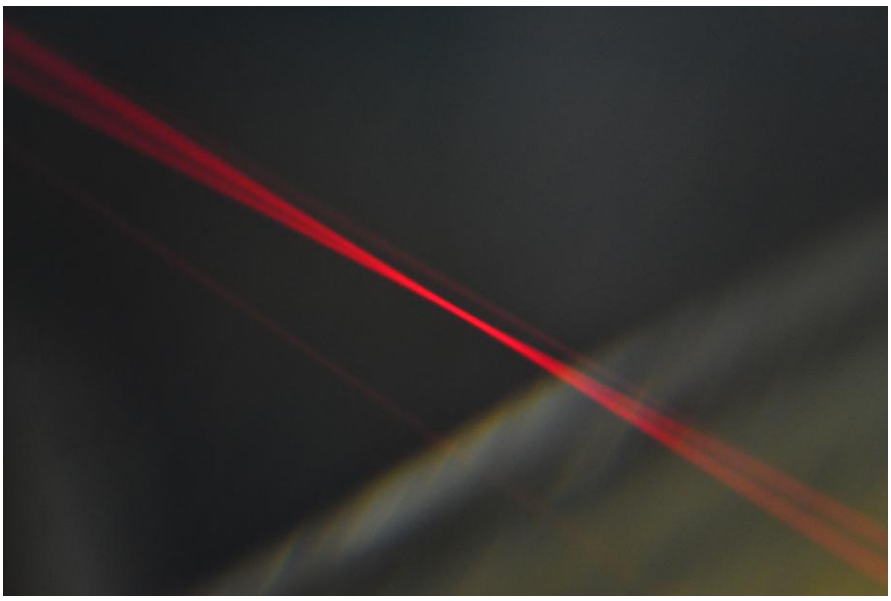

(a) Photo of the beams crossing, as seen from above.

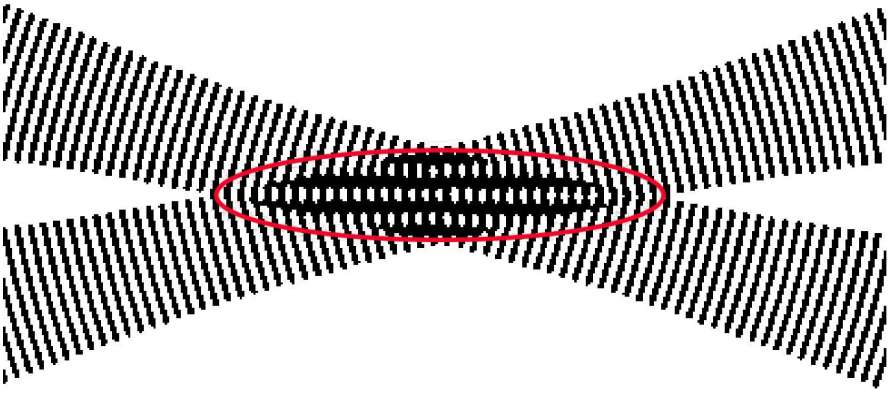

(b) Sketch of the Young's interference fringes when the beams cross.

Figure 7: Beam crossing.

Besides calculating the frequency from the scattered light, the small angle (θ) that the two beams make upon crossing must also be determined. This angle was calculated by reflecting with a mirror the beams before crossing. The beams were directed to a wall, creating a triangle between the crossing beams and the wall. Then, by measuring the sides of such triangle and applying the cosine theorem, θ can be calculated. The cosine theorem is defined as:

$$c^2 = a^2 + b^2 - 2ab\,cos(\theta) \qquad \text{so that} \qquad \theta = cos^{-1}\left(\frac{a^2 + b^2 - c^2}{2ab}\right) \tag{2}$$

The geometry of the procedure is sketched in Fig. (8).

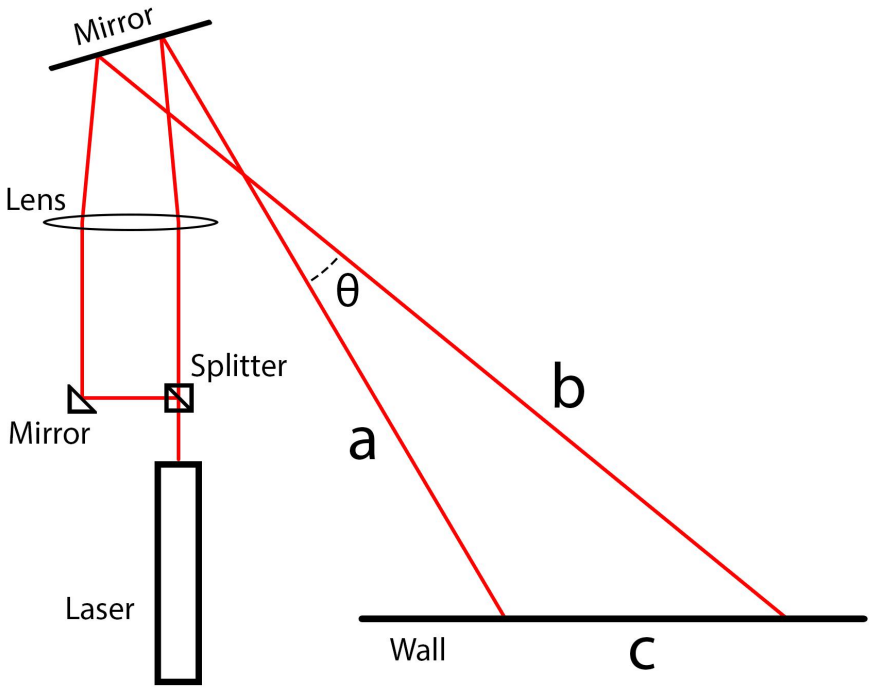

Figure 8: Geometry used to calculate the intersecting angle of the beams, θ.

The procedure to calculate the velocity was as follows. First of all, the following data had to be collected:

- Obtain the frequency (f) of the interference signal.
- Measure the angle (θ) between the crossing beams.
- Know the wavelength (λ) of the light emitted from the laser.

Then, the absolute velocity of a particle in the flow could be calculated with Eq. (3):

$$U_{LDV} = \frac{f\,\lambda}{2\,sin(\theta/2)} \tag{3}$$

Since the measurements of the frequency and the angle have initial uncertainties (Δf and $\Delta\theta$), they are propagated to the velocity calculation and must be taken into account. It must be noted that the wavelength of the laser light was a given quantity and it was assumed to be measured with an infinite precision ($\Delta\lambda = 0$). Although it is impossible to measure any quantity with a zero uncertainty, it is a fair assumption since the error in the measurement of λ would be negligible compared with the errors given by the frequency and θ. Thus, using Eq. (1), the propagated error in the velocity of the flow can be calculated.

$$\Delta U_{LDV} = \sqrt{(\Delta U_f)^2 + (\Delta U_\theta)^2} = \sqrt{\left[\left(\frac{\partial U}{\partial f}\right)\Delta f\right]^2 + \left[\left(\frac{\partial U}{\partial \theta}\right)\Delta\theta\right]^2} = \sqrt{\left(U\,\frac{\Delta f}{f}\right)^2 + \left(\frac{U}{2}\,\frac{\Delta f}{tan(\theta/2)}\right)^2} \tag{4}$$

Therefore, Eq. (4) was used in order to calculate how the initial uncertainties of the measured parameters f and θ were propagated into the velocity of the flow.

3.4 Velocity distribution functions and root mean square velocity in the free stream

It was found that not all the particles in a fixed free stream velocity move at the same velocity. In order to model how the velocities of the measured particles vary, two different probability distribution functions were considered.

For a given probability density function $F(U)$, the probability is defined as the area below the curve described by such function. Thus, the probability of finding a particle whose velocity lies in the velocity range $[U_0, U_0 + \delta U_0]$ can be calculated as:

$$\mathbb{P} = \int_{U_0}^{U_0+\delta U_0} F(U)\, dU \tag{5}$$

Another parameter that can be calculated for a set of different velocities is the root mean square velocity. In order to do so, the perturbations in velocity must be defined (U'). Such parameter is defined as the difference between the velocity (U) and the mean velocity ($\overline{U}$):

$$U' = U - \overline{U} \tag{6}$$

Then, the root mean square speed is defined as:

$$U_{rms} = \sqrt{\int_{-\infty}^{+\infty} (U')^2\, F(U)\, dU} \tag{7}$$

3.4.1 Experimental data analysis

In order to compare the experimental data with the predicted velocity distributions, Eqs. (5) and (7) must be modified for a finite sample of velocities. The probability and root mean square velocity can be simply calculated as follows:

$$\mathbb{P} = \frac{\text{Number of samples that lay inside range } U_0 \text{ and } U_0 + \delta U_0}{N} \tag{8}$$

$$U_{rms} = \sqrt{\frac{1}{N}\left(\sum_{i=1}^{N} (U_i - \overline{U})^2\right)} \tag{9}$$

Also, the mean velocity ($\overline{U}$) and variance (σ^2) are calculated from the experimental data, which were used as input parameters in the different velocity distributions described below.

3.4.2 Normal distribution

The shape of a normal distribution function is given by the following equation [5]:

$$F_N(U) = \frac{1}{\sqrt{2\pi\sigma^2}} \cdot exp\left[- \frac{(U - \overline{U})^2}{2\sigma^2} \right] \tag{10}$$

A graphical representation of Eq. (10) for different values for $\overline{U}$ and σ^2 can be observed in Fig. (9).

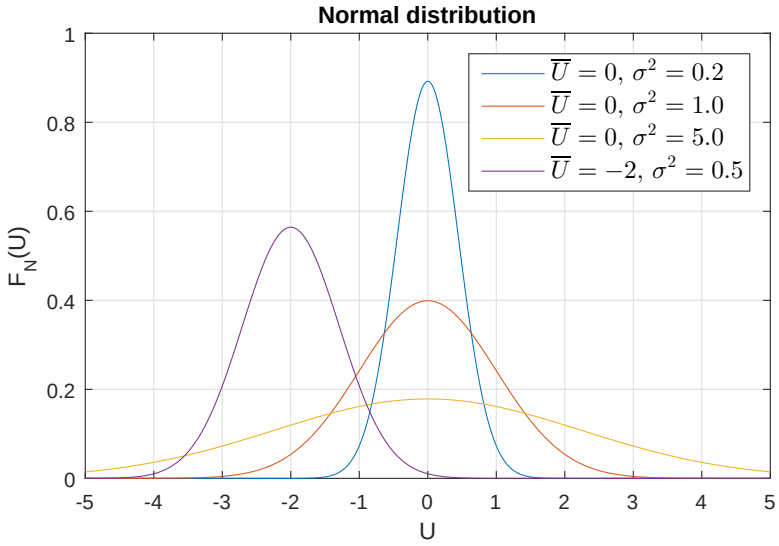

Figure 9: Normal distribution as a function of different values of $\overline{U}$ and σ^2.

Then, introducing the definition of $F_N(U)$ from Eq. (10) into Eq. (5), an expression that predicts the probability of finding a particle in a given velocity range was obtained. The procedure followed to obtain such probability is displayed below:

$$\mathbb{P}_N = \int_{U_0}^{U_0+\delta U_0} \frac{1}{\sqrt{2\pi\sigma^2}} \cdot exp\left[-\frac{(U-\overline{U})^2}{2\sigma^2}\right] dU \quad \rightarrow$$

$$\rightarrow \quad \mathbb{P}_N = \left[-\frac{1}{2} erf\left(\frac{U-\overline{U}}{\sigma\sqrt{2}}\right)\right]_{U_0}^{U_0+\delta U_0} \quad \rightarrow$$

$$\rightarrow \quad \mathbb{P}_N = \frac{1}{2}\left[erf\left(\frac{(U_0+\delta U_0)-\overline{U}}{\sigma\sqrt{2}}\right) - erf\left(\frac{U_0-\overline{U}}{\sigma\sqrt{2}}\right)\right] \tag{11}$$

Also, the root mean square velocity for the normal distribution function is calculated using Eq. (7). The procedure followed to obtain the final expression for U_{rms} is displayed below:

$$U_{rmsN} = \sqrt{\int_{-\infty}^{+\infty} \frac{(U-\overline{U})^2}{\sqrt{2\pi\sigma^2}} \cdot exp\left[-\frac{(U-\overline{U})^2}{2\sigma^2}\right] dU} \quad \rightarrow$$

$$\rightarrow \quad U_{rmsN} = \sqrt{\left[\frac{\sigma}{\sqrt{2\pi}}(\overline{U}-U)^2 \cdot exp\left(-\frac{(U-\overline{U})^2}{2\sigma^2}\right) - \frac{\sigma^2}{2} \cdot erf\left(\frac{\overline{U}-U}{\sqrt{2}\sigma}\right)\right]_{-\infty}^{+\infty}} \quad \rightarrow$$

$$\rightarrow \quad U_{rmsN} = \sqrt{\sigma^2 + \left[\lim_{U\to+\infty} \frac{\sigma}{\sqrt{2\pi}}(\overline{U}-U)^2 \cdot exp\left(-\frac{(U-\overline{U})^2}{2\sigma^2}\right)\right]^{0} - \left[\lim_{U\to-\infty} \frac{\sigma}{\sqrt{2\pi}}(\overline{U}-U)^2 \cdot exp\left(-\frac{(U-\overline{U})^2}{2\sigma^2}\right)\right]^{0}} \quad \rightarrow$$

$$\rightarrow \quad U_{rmsN} = \sigma \tag{12}$$

Finally, it was found that, for a normal velocity distribution function, the root mean square of the velocity is simply the standard deviation (σ) of the set of samples taken.

3.4.3 Weibull distribution

The shape of the Weibull function is given by the following equation [6]:

$$F_W(U) = \begin{cases} \frac{k}{\xi}\left(\frac{U}{\xi}\right)^{k-1} \cdot exp\Big[-\left(\frac{U}{\xi}\right)^{k}\Big] & U \geq 0 \\ 0 & U < 0 \end{cases} \tag{13}$$

A graphical representation of Eq. (13) for different values of ξ and k can be observed in Fig. (10).

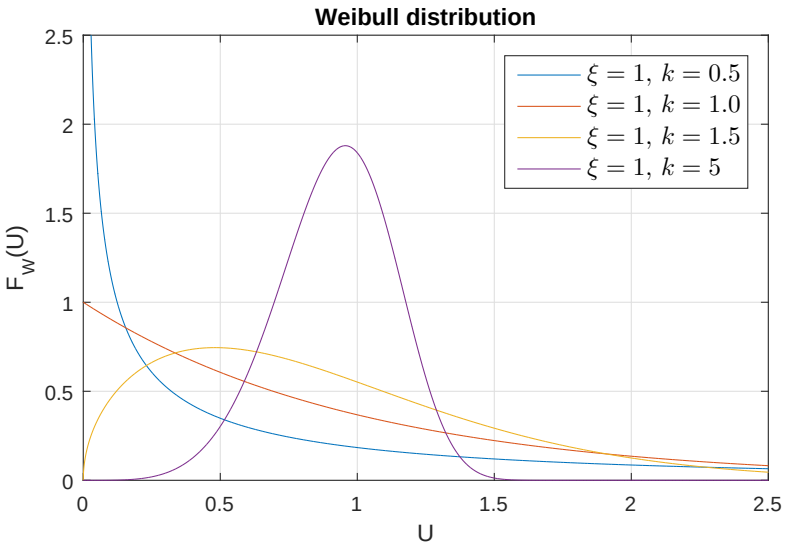

Figure 10: Weibull distribution as a function of different values for ξ and k.

For this probability density function, the parameters k and ξ are related to the mean and variance in the following manner:

$$\overline{U} = \xi \cdot \Gamma\left(1 + \frac{1}{k}\right) \tag{14}$$

$$\sigma^2 = \xi^2 \left[\Gamma\left(1 + \frac{2}{k}\right) - \left(\Gamma\left(1 + \frac{1}{k}\right)\right)^2\right] \tag{15}$$

where $\Gamma(z)$ is the Gamma function [7], defined as: $\Gamma(z) = \int_0^{+\infty} x^{z+1} \cdot e^{-x} dx$.

Following a similar procedure to what was done for the normal distribution, it can be shown that the probability of finding a particle inside the velocity element $[U_0, U_0 + \delta U_0]$ is given by the following expression:

$$\mathbb{P}_W = \int_{U_0}^{U_0+\delta U_0} \frac{k}{\xi}\left(\frac{U}{\xi}\right)^{k-1} \cdot exp\left[-\left(\frac{U}{\xi}\right)^{k}\right] dU = exp\left[-\left(\frac{U_0}{\xi}\right)^{k}\right] - exp\left[-\left(\frac{U_0 + \delta U_0}{\xi}\right)^{k}\right] \tag{16}$$

As for the root mean square velocity, the procedure followed to derive its equation is given by:

$$U_{rmsW} = \int_0^{+\infty} (U - \overline{U})^2 \frac{k}{\xi}\left(\frac{U}{\xi}\right)^{k-1} \cdot exp\left[-\left(\frac{U}{\xi}\right)^{k}\right] dU = \sigma \tag{17}$$

As it can be observed in Eq. (17), for the Weibull distribution the root mean square velocity is equal to the standard deviation. It must be noted that this is the same result given by the normal distribution function, as shown in Eq. (12).

3.5 Water physical properties

Measuring all the physical properties of the water is not a trivial process. Therefore, in order to calculate the viscosity and density of the water, curve-fits that are function of only the temperature were used [8]. In these curve-fits the temperature must be inputted in degrees Celsius, $T = [^oC]$, and the final result is given in SI units.

The density, $\rho = [kg/m^3]$, is defined as:

$$\rho = \frac{999.83952 + 16.945176\,T - 7.9870401 \cdot 10^{-3}\,T^2 - 46.170461 \cdot 10^{-6}\,T^3 + 105.56302 \cdot 10^{-9}\,T^4 - 280.54253 \cdot 10^{-12}\,T^5}{1 + 16.879850 \cdot 10^{-3}\,T} \tag{18}$$

The viscosity, $\mu = [kg/(m \cdot s)]$, has different expressions depending on the temperature range.

- For $(0 < T < 20^oC)$, the viscosity is defined as:

$$\mu = 10^{-3} \cdot 10^{A} \qquad \text{where} \qquad A = \frac{1301}{998.333 + 8.1855 \cdot (T-20) + 0.00585 \cdot (T-20)^2} - 1.30223 \tag{19}$$

- For $(20 < T < 100^oC)$, the viscosity is defined as:

$$\mu = 1.002 \cdot 10^{-3} \cdot 10^{B} \qquad \text{where} \qquad B = \frac{1.3272 \cdot (T-20) - 0.001053 \cdot (T-20)^2}{T + 105} \tag{20}$$

Fig. (11) shows the distribution of these curve-fits as a function of the temperature. Therefore, by using the previous curve-fits, all the required physical properties of the water were known by only measuring its temperature.

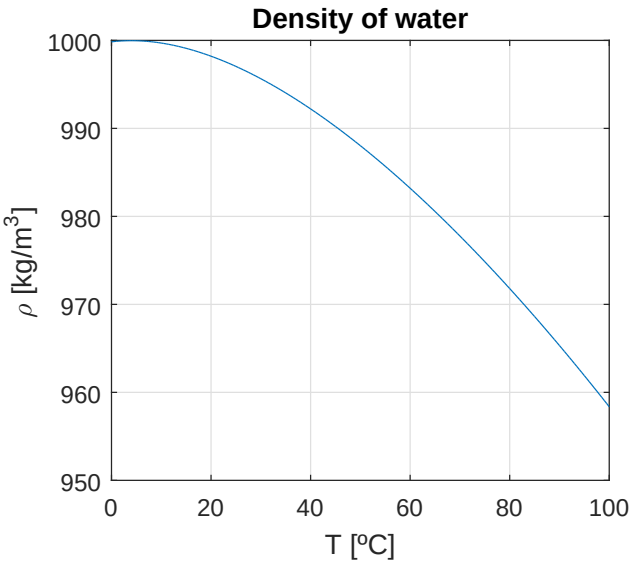

(a) Density of the water over a range of temperatures.

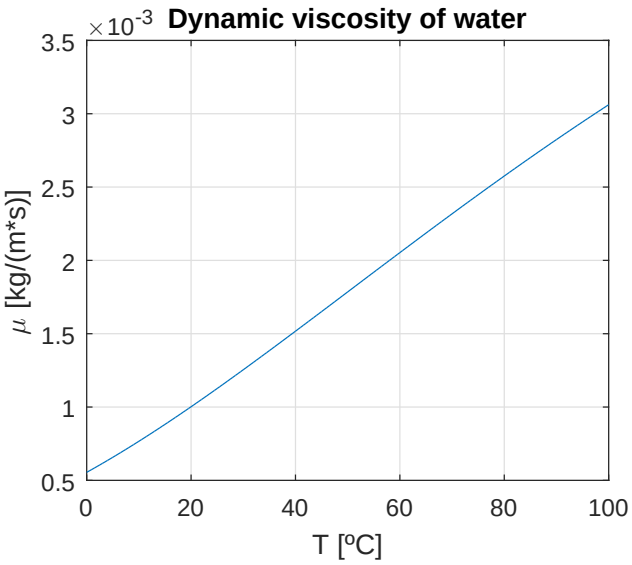

(b) Dynamic viscosity of the water over a range of temperatures.

Figure 11: Density and dynamic viscosity of the water as a function of the temperature according to the curve-fits from [8].

3.6 Flow regimes

The different flow regimes observed in the flow visualization can be differentiated in terms of the Reynolds number. The Reynolds number is physically a measure of the ratio of inertia forces to viscous forces in a flow, and is one of the most powerful parameters in fluid dynamics [4]. This ratio can be expressed as:

$$Re = \frac{\rho\, U\, l_c}{\mu} \tag{21}$$

The uncertainty in the Reynolds number can be calculated applying Eq. (1). Thus, the error in Re is:

$$\Delta Re = Re \sqrt{\left(\frac{\Delta\rho}{\rho}\right)^2 + \left(\frac{\Delta U_\infty}{U_\infty}\right)^2 + \left(\frac{\Delta l_c}{l_c}\right)^2 + \left(\frac{\Delta\mu}{\mu}\right)^2} \tag{22}$$

where the error in dynamic viscosity and density can be computed as follows, since they are only a function of the temperature.

$$\Delta\mu = \left|\frac{d\mu}{dT}\,\Delta T\right| \qquad \text{and} \qquad \Delta\rho = \left|\frac{d\rho}{dT}\,\Delta T\right| \tag{23}$$

The parameter that determines the flow regime in subsonic conditions is the local Reynolds number, which depends on the downstream location of the fluid as it passes around an object. This parameter increases as the flow moves around an object, allowing the flow to change from one regime to another. Thus, the local Reynolds number is defined as:

$$Re_x = \frac{\rho\, U\, x}{\mu} \tag{24}$$

Depending on the value of the Reynolds number, three different flow regimes can be identified. These regimes are laminar flow, turbulent flow, and transitional flow [9].

3.6.1 Laminar flow

Laminar flow occurs when the fluid flows in an ordered manner, and the streamlines can be clearly defined. These streamlines do not disrupt each other and mixing does not occur. Typically, for laminar flow regimes, analytic solutions can be obtained and it can be easily observed experimentally. Also, laminar flow occurs at low local Reynolds numbers where viscous forces have a significant influence over the flow. Figure (12) shows how laminar flow behaves inside a pipe.

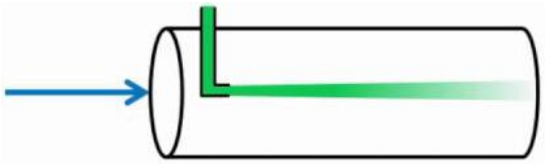

Figure 12: Laminar flow visualization diagram.

3.6.2 Turbulent flow

Turbulence is a highly unsteady and chaotic phenomenon in which the fluid undergoes irregular fluctuations, or mixing. In these turbulent regions the speed of the fluid at a point is continuously and randomly undergoing changes in

both magnitude and direction. This makes turbulence a very complex phenomenon, and difficult to be analyzed both analytically and experimentally. As a result, time-averaged quantities are typically used to solve most fluid mechanic problems dealing with turbulent flows. Turbulent flows occur at high local Reynolds number, where the inertial forces are dominant. Figure (13) shows how turbulent flow behaves inside a pipe.

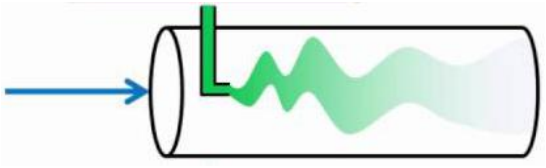

Figure 13: Turbulent flow visualization diagram.

3.6.3 Transitional flow

The transition from laminar to turbulent flow has been a matter of research over the years. When approaching the transition point, any small change in any of the properties of the flow can make it behave either turbulent or laminar. Due to this fact, the transition point does not always remain at the same location. Instead, it moves as a result of small fluctuations in the flow properties at a given instant. Nowadays it is still not possible to accurately determine where transition will occur. The transition point is estimated based on experience, previous experiments, and observation. Figure (14) shows how transitional flow behaves inside a pipe.

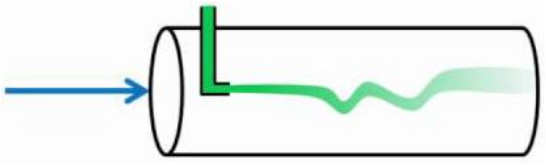

Figure 14: Transitional flow visualization diagram.

3.7 Wake

Whenever an object is moving relative to a real fluid, a flow pattern called wake is developed. Such wake is observed to form behind moving bodies at all speeds (except at $Re < 1$), and all flow regimes. For low speeds the flow is dominated by viscosity, and a recirculation region with a vortex or a pair of vortices is created downstream the object. For higher Reynolds numbers the wake is turbulent. This phenomenon can easily be visualized in the trailing wake behind boats as they sail through water, as seen in Fig. (15).

Figure 15: Boat sailing the Lyse fjord in Norway, in which the wake is clearly defined (Courtesy of *Edmont*).

4 Procedure

In the experimental session, data was acquireda using two different procedures. The first procedure was to use LDV in order to measure the velocity of the flow, and the second procedure was to perform flow visualization.

4.1 LDV setup

Before using the LDV, the angle between the two beams had to be calculated. In order to determine θ, the cosine theorem was applied, as described in Section (3.3). Once θ was calculated, measurements with the LDV could be taken. Fig. (16) displays the setup used in the experiment when measuring the velocity with the LDV.

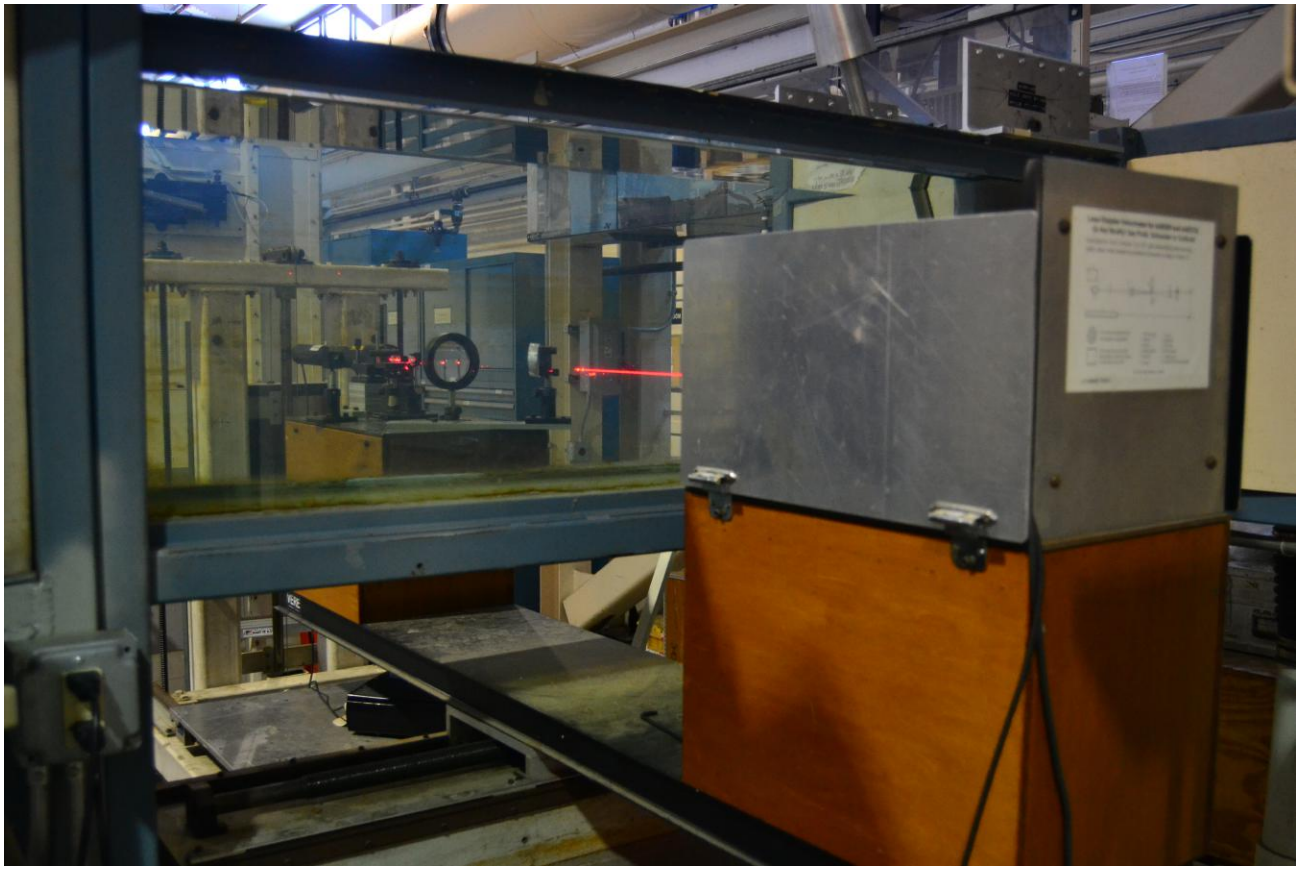

Figure 16: LDV setup, where the beams cross inside the tunnel.

As it can be observed in Fig. (16), the laser beams crossed in the water tunnel. Then, the signal transmitted to the oscilloscope, and amplified using a high-pass filter. Finally, the filtered signal was exported as a *.wfm* file in order to analyze it using *MATLAB*. A detailed explanation of how the signal was analyzed can be found in Section (5.2). Furthermore, according to [3], the wavelength of the beams from the laser was $\boldsymbol{\lambda = 633\ nm}$.

4.2 Flow visualization setup

Flow visualization was performed around the nosecone at different free stream velocities and angles of attack. The cone was submerged inside the water tunnel, adjusting its angle of attack with the digital magnetic angle gauge level. After adjusting the free stream velocity, blue dye was injected through the small holes of the cone. Fig. (17) displays the dye system used.

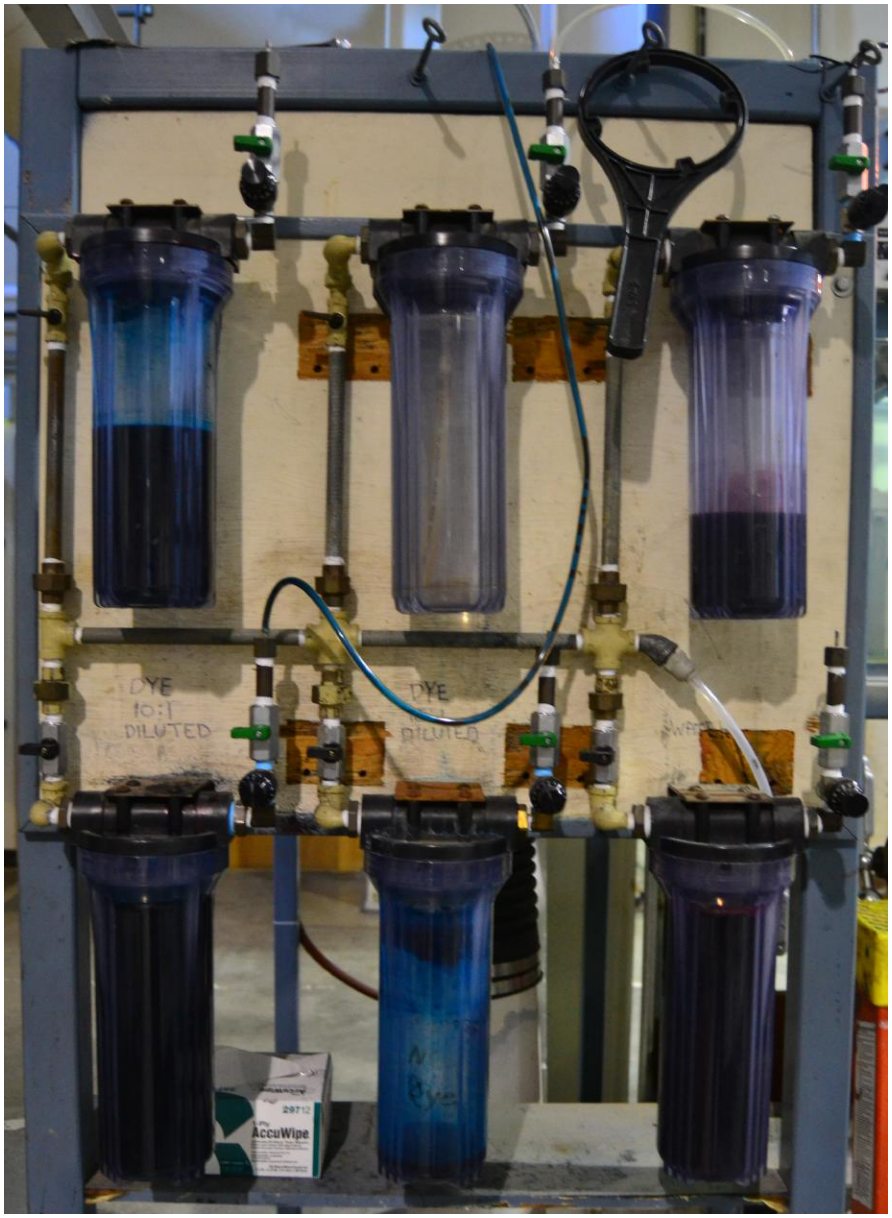

Figure 17: Dye system used to perform flow visualization.

Although in the figure there are 6 different containers, only 2 were used: 1 for the blue dye, and 1 for the water. Since the water tunnel was a closed-cycle tunnel, the water became progressively blue after injecting the dye. Therefore, the dye injected was mixed with water in order not to turn the entire tunnel blue too soon. Once the flow was being ejected from the small holes, pictures were taken in order to capture the different flow regimes. A white background was installed in order to increase the contrast of the dye with the background, which enhanced the quality of the photographs.

5 Analysis of Results

5.1 Beam intersection angle

The beam intersection angle was measured following the procedure explained in Section (3.3). Since the final value of θ was very sensitive to the measurements of the triangle sides, they were measured multiple times in order to get a more precise result. Table (1) displays all the different measurements taken, where a, b and c are the sides of the triangle displayed in Fig. (8).

Measurement	a $[m]$	b $[m]$	c $[m]$	θ [°]
1	2.65	2.69	0.152	3.15
2	2.60	2.66	0.151	3.02
3	2.64	2.70	0.152	3.00
4	2.65	2.72	0.151	2.86
5	2.70	2.76	0.152	2.93

Table 1: Measurements taken to calculate the beam intersection angle θ.

Then, the final value of θ was computed by averaging the different θ values obtained. As of the uncertainty in the angle, $\Delta\theta$, it was defined as the greatest difference between the mean and each calculated angle. Therefore, the final values were $\boldsymbol{\theta = 2.99}^{\circ}$, and $\boldsymbol{\Delta\theta = 0.16}^{\circ}$.

5.2 Signal analysis

In order to analyze the signal coming from the LDV, a high-pass filter was used. Sometimes, however, this high-pass filter would overload during the data acquisition process. Upon this occurrence, the high-passed signal did not make physical sense and such measurement had to be discarded. Fig. (18) shows the high pass filter overloaded.

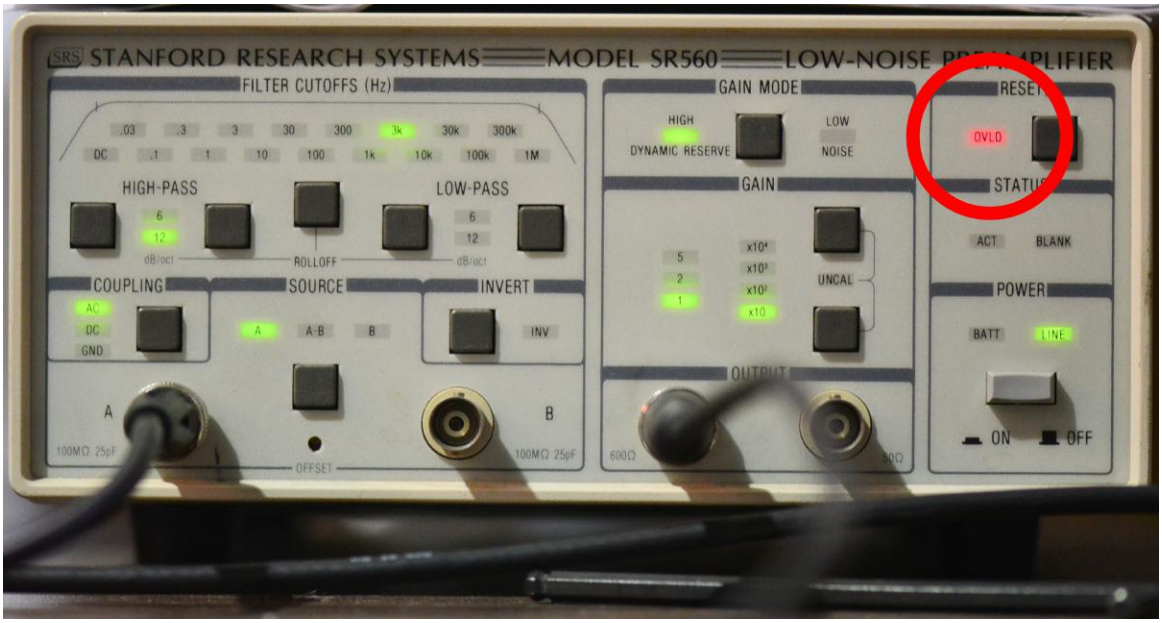

Figure 18: High-pass filter overloaded.

The signal was analyzed using Fast Fourier Transform (FFT) in *MATLAB* with the built-in function $Y = fft(X)$. The FFT is a mathematical transformation that computes the amplitude of each frequency for a given signal. This allows to identify the dominant frequency over the noise of the signal. Fig. (19) displays the raw and high-passed signals, and Fig. (20) displays the FFT analysis of that signal.

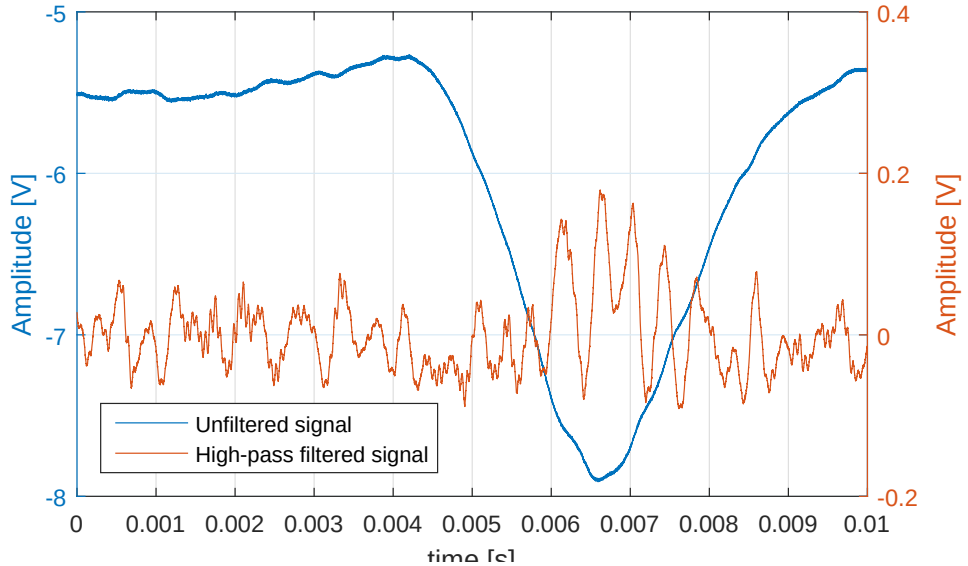

Figure 19: LDV raw and filtered signals of a particle crossing the laser beams.

The drop in voltage of the unfiltered signal of Fig. (19) shows that there was a particle that crossed the LDV laser beams. Also, the high-pass filtered signal shows an increase in amplitude as the particle passed, which was where the frequency would be determined. This frequency was expected to appear as a single peak in amplitude of the signal after applying the FFT. However, after analyzing the signal, in almost every case two dominant frequencies appeared as it can be observed from the two peaks in Fig. (20).

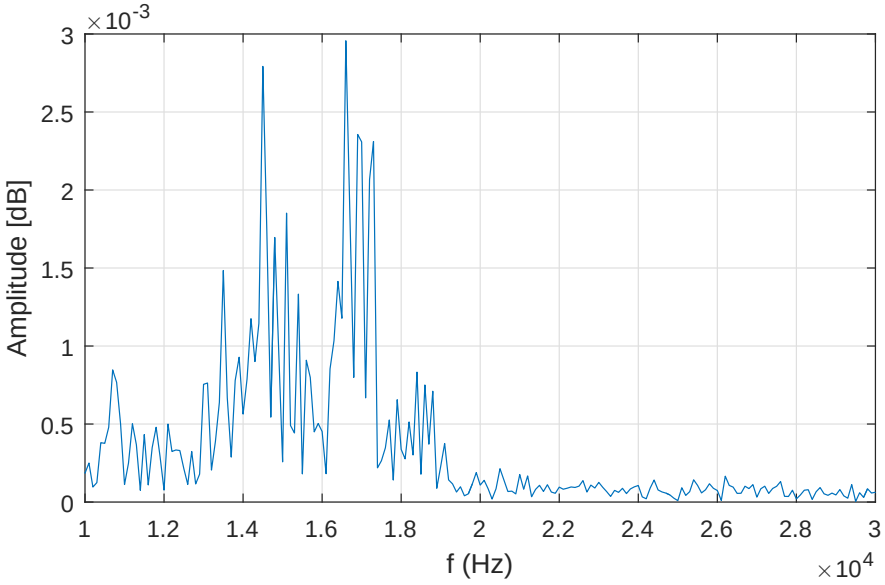

Figure 20: Fast Fourier transform of the high-passed signal from Fig. (19).

As this method did not give a conclusive result, some frequencies were also calculated "by eye" to determine a pattern of which of the two peaks was the real solution and which one was noise. An example of calculating the frequency "by eye" of the high-passed signal in Fig. (19) is given below.

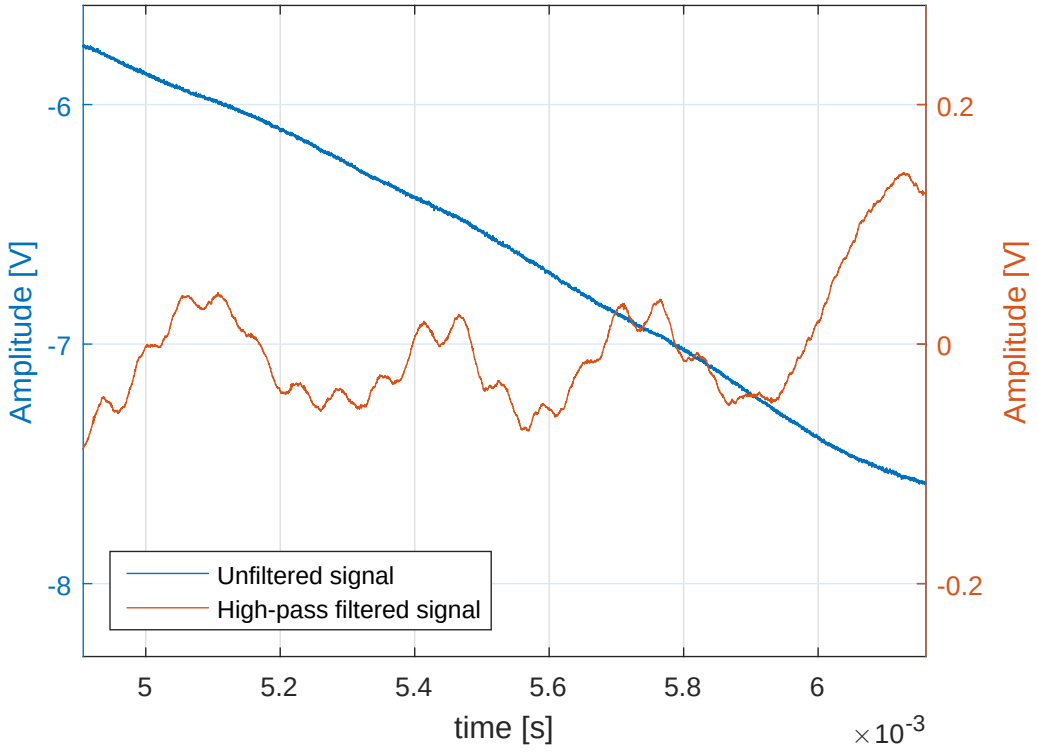

Figure 21: Closeup of Fig. (19).

The frequency was calculated by counting the number of peaks over a period of time. By inspecting Fig. (21), a total of 10 peaks were spotted over a period of 0.6 ms (from $t = 5.2\,ms$ to $t = 5.8\,ms$), which gave the following frequency.

$$f_{eye} = \frac{10\,[peaks]}{(5.8 - 5.2) \cdot 10^{-3}\,[s]} = 16.7\,kHz \tag{25}$$

The frequency calculated "by eye" resembles better the second peak frequency of Fig. (19) rather than the first peak. Therefore, it was decided that the most accurate frequency solution to use was the second frequency peak in every FFT signal. However, this assumption implies a big uncertainty. In order to be conservative, it was determined that the frequency uncertainty would be the largest difference between the 2 peaks from all samples taken, which was $\boldsymbol{\Delta f = 2.3\,kHz}$.

5.3 LDV velocity comparison with the flowmeter velocity

In order to determine if the built-in flowmeter was correctly calibrated, flow velocity in the free stream was measured using the flowmeter and LDV for different water tunnel speeds. For each flowmeter speed, three different LDV measurements were taken in order to get a more precise result. These three measurements for each flowmeter velocity are displayed in Fig. (22).

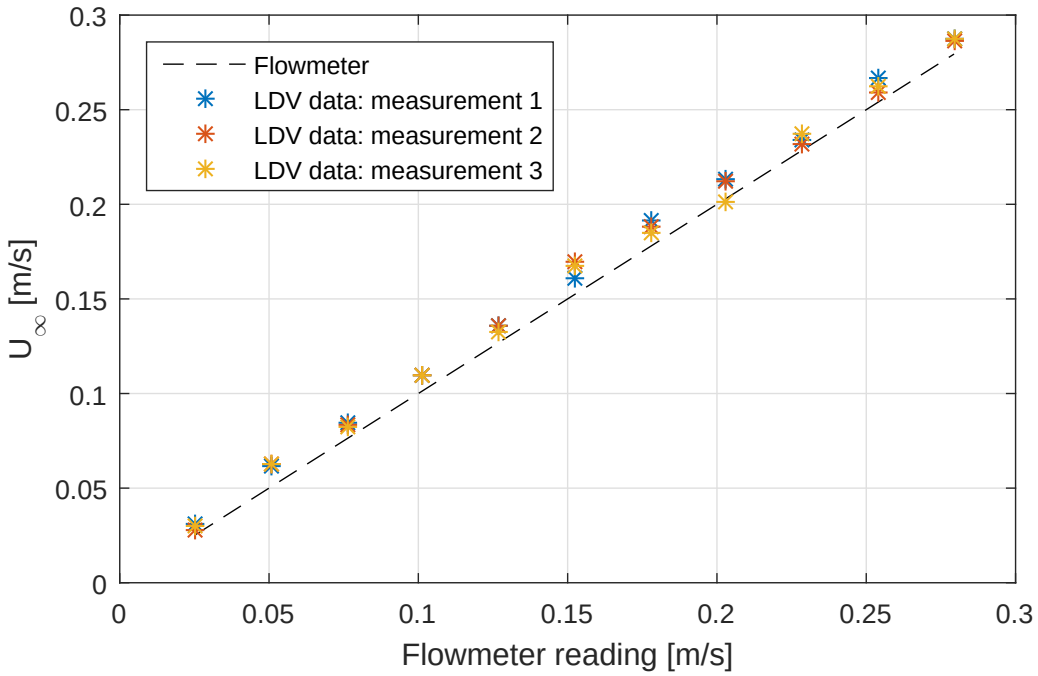

Figure 22: Different LDV velocity readings compared with the flowmeter velocities.

The average of the three different measurements, as well as a linear-fit of them is displayed in Fig. (23). Furthermore, error bars have been added, which correspond to the maximum error either from the error propagation from Eq. (4), or the distance between one of the three measurements from its average.

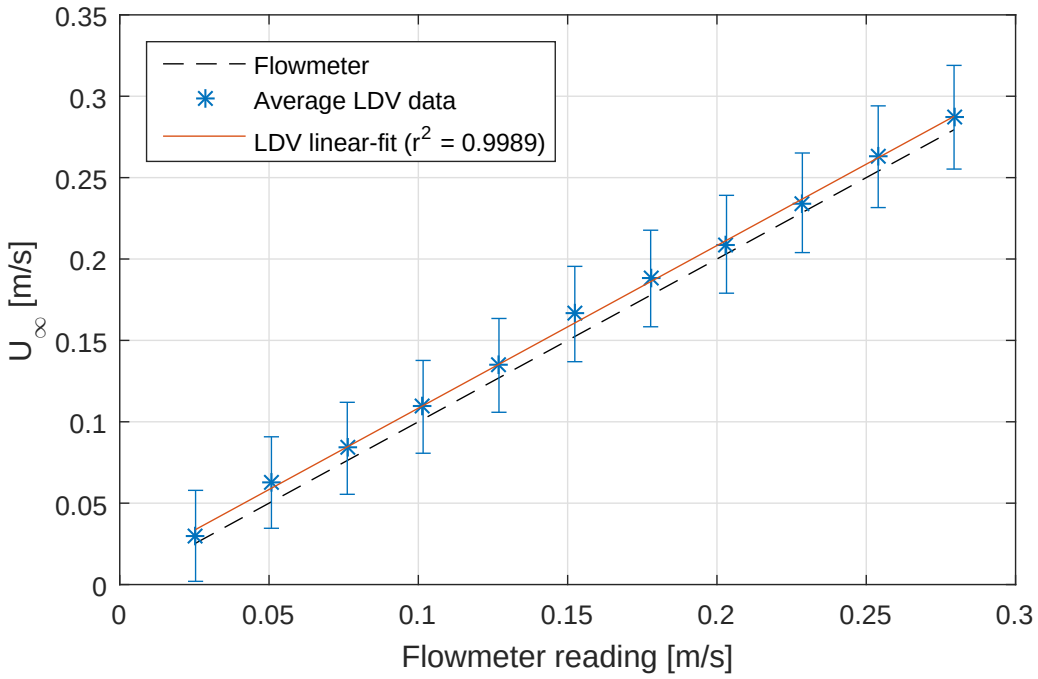

Figure 23: Mean LDV velocity readings with linear-fit compared with the flowmeter velocities.

As it can be observed in Fig. (22) and Fig. (23) velocity given by the flowmeter and by the LDV are very similar. Almost every LDV velocity laid slightly above the flowmeter velocity, and the flowmeter values are well within the error bars. Furthermore, the linear-fit of the LDV velocities is compared with the flowmeter velocity, and it is displayed in Table (2). The goal of making a linear-fit was to obtain an equation that related the flowmeter velocity reading with the actual free stream velocity. The actual free stream velocity was assumed to be the LDV velocity, since the LDV measures absolute velocities.

Measuring device	Linear-fit
Flowmeter $[m/s]$	$U_\infty = U_{flowmeter}$
LDV $[m/s]$	$U_\infty = 0.9994 \cdot U_{flowmeter} + 0.0084$

Table 2: Linear-fit for the free stream velocity compared with the flowmeter velocity.

As it can be observed in Table (2), the flowmeter velocity is equal to the free stream velocity ($U_\infty = U_{flowmeter}$). Even though this might not be true, this was done in order to set the flowmeter as the reference velocity.

The slope of the LDV linear fit was almost equal to one ($0.9994 \cong 1$), and there was a small offset of $0.0084\, m/s$. This means that every LDV velocity was almost $0.0084\ m/s$ above the flowmeter velocity, which is the behaviour observed in Figs. (22) and (23). Nevertheless, a difference of $0.0084 m/s$ in the velocity readings was reasonably small, and suggested that both methods worked correctly.

Furthermore, it must be noted that the error bar contribution for the LDV measurements was almost equally split between ΔU_f and ΔU_θ. Since a high Δf was caused by having two peaks in the FFT transformations, both uncertainties were comparable $\Delta U_f \approx \Delta U_\theta$. However, if there were only one clear dominant frequency in the FFT for the velocities, Δf could have been significantly decreased. Thus, the largest contribution to the total uncertainty in the velocity would have come from the beam intersecting angle error, ΔU_θ.

5.4 Velocity distribution functions

The aim of this section is to statistically study the distribution of particles in the free stream as a function of their velocity. In order to do so, two probability distribution functions were considered: normal distribution function and Weibull distribution function. Also, the free stream velocity was assumed to be the the mean velocity for each case ($U_\infty = \overline{U}$). The input for both distribution functions were the mean and variance parameters, from each case analyzed. In order to validate the distributions, the probability of finding a particle within a certain velocity range was calculated. Then, it was compared with its actual experimental probability. These quantities were calculated following the procedure described in Section (3.4).

Four different cases were analyzed, each of them with a sample size of 50 velocities, at increasing free stream velocities. The probabilities of finding a particle with a certain velocity over a given range of velocities is displayed on each figure. They have been calculated for each probability distribution, as well as from experimental data. Figs. (24), (25), (26) and (27) display each case for increasing free stream velocity.

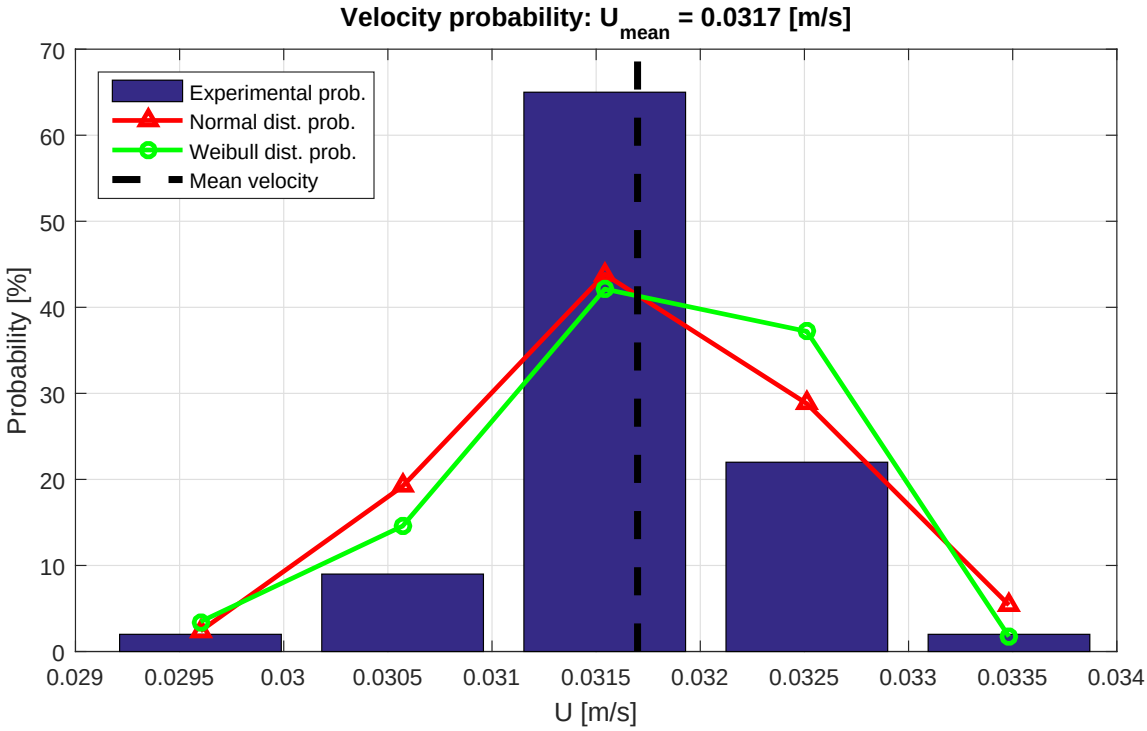

Figure 24: Velocity distribution comparison: Case 1.

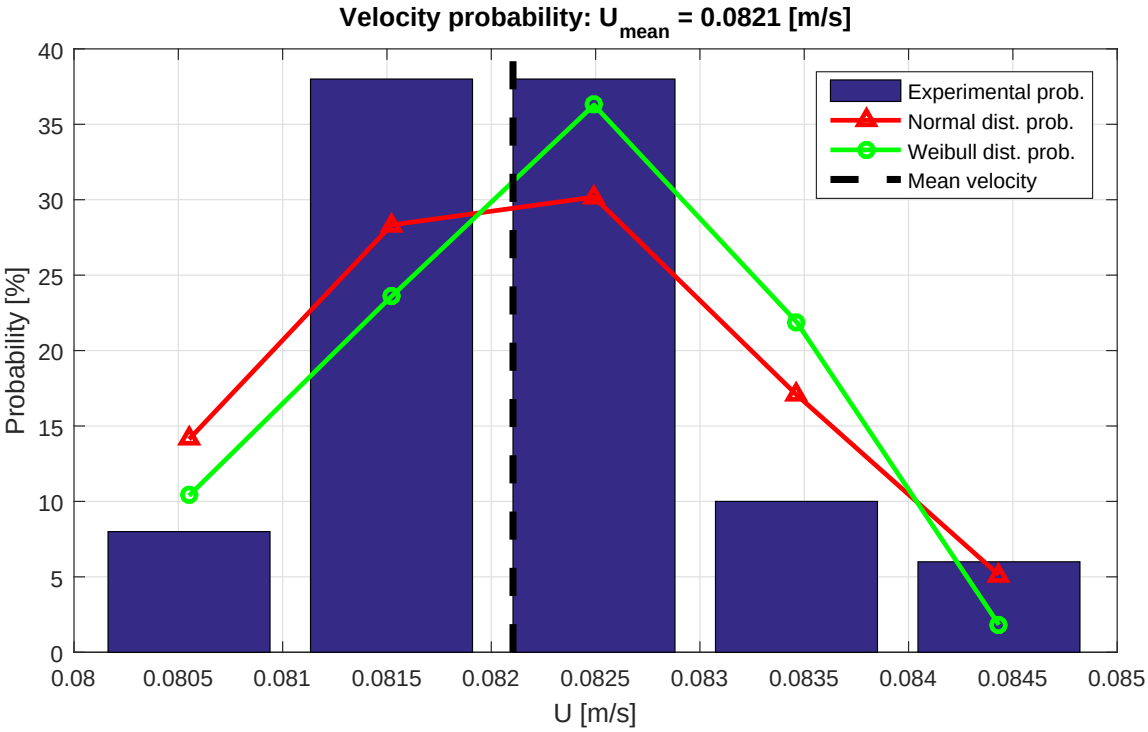

Figure 25: Velocity distribution comparison: Case 2.

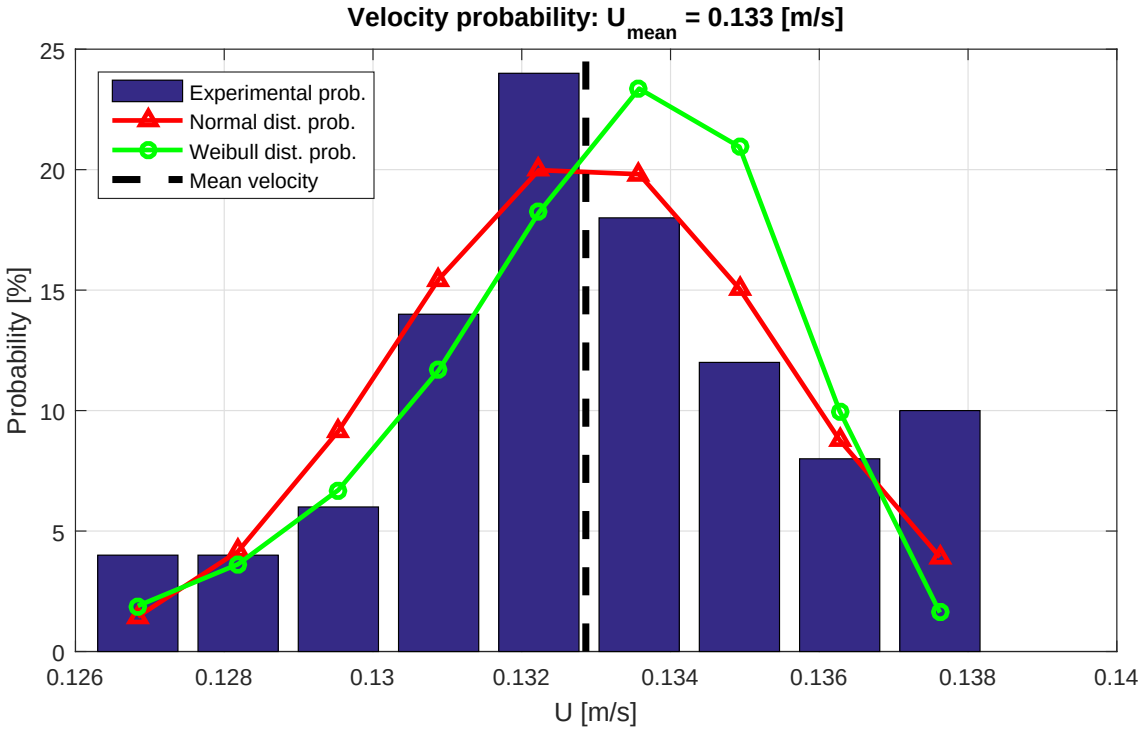

Figure 26: Velocity distribution comparison: Case 3.

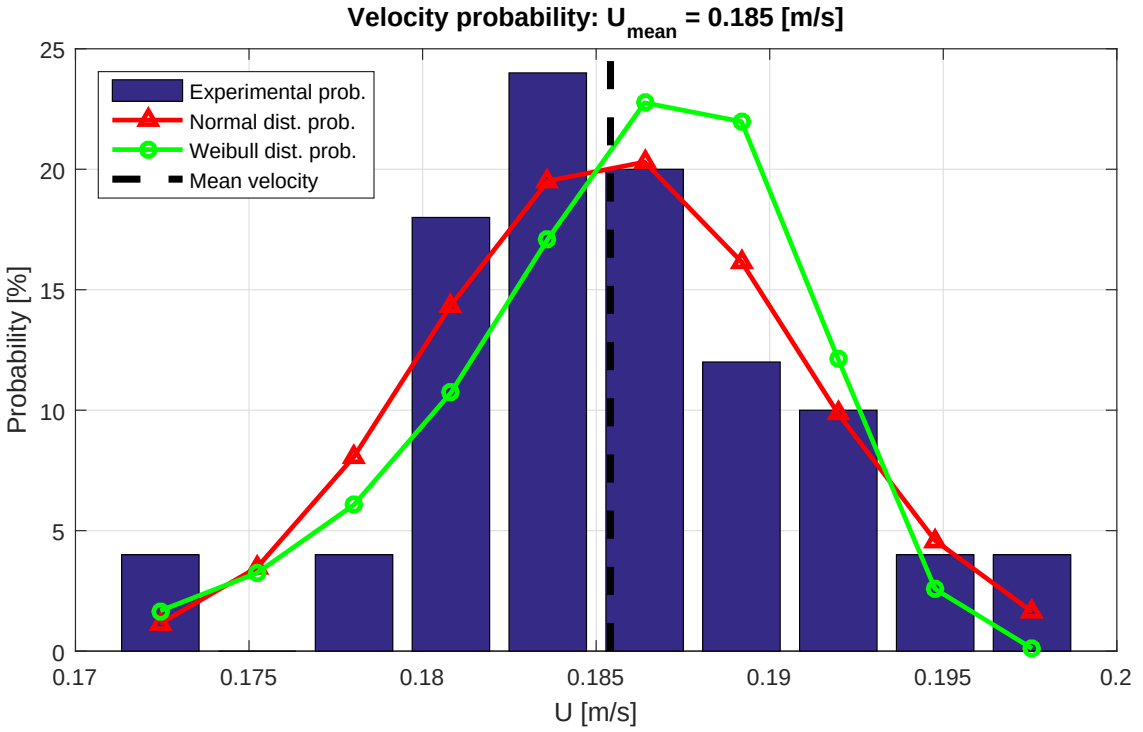

Figure 27: Velocity distribution comparison: Case 4.

In Figs. (24) and (25) a total of 5 velocity intervals were used, and in Figs. (26) and (27) 9 and 10 respectively. This was a result of the frequency resolution, which directly determined the velocity resolution. When obtaining data from the LDV, frequency was a discrete variable whose step depends on the sampling frequency. This meant that not

all frequencies were measured, so the result was approximated to the nearest value. The effect of this approximation is more noticeable at low velocities where the frequency is lower. As a result, the normal and Weibull distribution functions better correlated for higher free stream velocities (cases 3 and 4) than for lower free stream velocities (cases 1 and 2). The mean free stream velocity, the variance of the sample set, and the two coefficients used for the Weibull distribution for each case studied are displayed in Table (3).

Case	$\overline{U}$ $[m/s]$	σ^2 $[m^2/s^2]$	k $[-]$	ξ $[m/s]$
1	0.0317	$0.6735 \cdot 10^{-6}$	48.822	0.0321
2	0.0821	$1.4080 \cdot 10^{-6}$	88.022	0.0826
3	0.1329	$6.6820 \cdot 10^{-6}$	65.201	0.1340
4	0.1854	$28.434 \cdot 10^{-6}$	43.883	0.1878

Table 3: Input values for the normal and Weibull distribution functions for each case studied

From analyzing Figs. (24), (25), (26) and (27), it was found that the normal distribution better described the experimental data than the Weibull distribution. This was due to the fact that the distributions of experimental velocities were almost symmetric. The Weibull distribution is not symmetric, so it estimates a maximum in probability after the mean velocity, which does not match the experimental results. In almost every case, it was found that the mean laid inside the bar with the highest probability, which is what the normal distribution predicts. However, the maximum probability estimated by the Weibull distribution had a better resemblance to the maximum obtained experimentally.

Overall, the distribution of particles as a function of the velocity is more accurately described by the normal distribution than by the Weibull distribution. Another important conclusion that can be obtained from this analysis is that very few measurements are needed to get an accurate result. Even if only one measurement is taken, the probability of being accurate up to the second decimal is extremely high.

The root mean square of the velocity fluctuations for each case was also studied. For both analytic models U_{rms} is equal to the standard deviation, as shown in Eqs. (12) and (17). Then, the experimental root mean square value for the velocity was calculated with Eq. (9). It is important to notice that U_{rms} had a value different from zero, which means that the free stream is not a perfectly unperturbed uniform flow. This means that even the free stream has some turbulence.

Case	Experimental (U_{rms}/U_∞) [%]	Theoretical (U_{rms}/U_∞) [%]	Error [%]
1	2.576	2.589	0.501
2	1.431	1.445	1.005
3	1.926	1.946	1.005
4	2.847	2.876	1.005

Table 4: Root mean square velocity comparison for each case.

Furthermore, curve-fits for U_{rms} and U_{rms}/U_∞ were done in order to interpolate among the experimental results. It must be noticed that the number of points used to create the curve-fit is not very high, so the validity of such curve-fit is limited. The curve-fit made for U_{rms} was a 6^{th} order polynomial with a minimum at $U_\infty = 0$. Using the built-in curve-fit generator in *MATLAB*, the equation given was:

$$\begin{aligned} U_{rms} = &- 77.2619 \cdot (U_\infty)^6 + 3.1889 \cdot 10^{-14} \cdot (U_\infty)^5 + 5.8337 \cdot (U_\infty)^4 - 1.4579 \cdot 10^{-15} \cdot (U_\infty)^3 + \\ &+ 0.021348 \cdot (U_\infty)^2 + 1.3879 \cdot 10^{-17} \cdot (U_\infty) + 7.8932 \cdot 10^{-4} \end{aligned} \tag{26}$$

The distribution of this curve-fit, as well as U_{rms}/U_∞ can be visualized in Fig. (28).

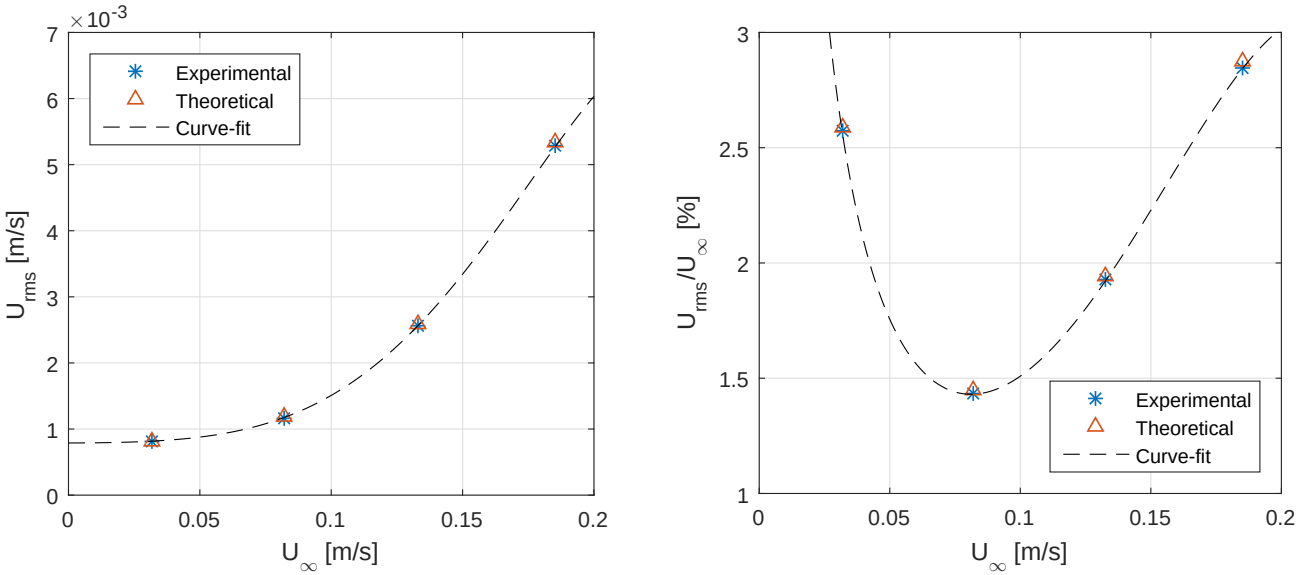

(a) U_{rms} curve-fit from experimental data.

(b) U_{rms}/U_∞ curve-fit from experimental data.

Figure 28: Curve-fits for the root mean square velocity data.

According to Fig. (28a) the velocity fluctuations reach a steady value for low velocity values and it increases as the free stream velocity increases. That is why in Fig. (28b) is possible to see an asymptotic behavior when the function approaches $U_\infty = 0$. It can also be observed that for high U_∞ values, the percentage of the velocity fluctuations increases, which implies that the flow in the free stream is more turbulent. Thus, a minimum value for U_{rms}/U_∞ must exist, which in Fig. (28b) lays at the second experimental sample $U_\infty = 0.0821\ m/s$. However, this is an approximation of the real case and more experimental data is required to determine where this minimum value is. Ideally, the water tunnel should be run at this speed whenever minimizing the effect of perturbations in the free stream is required.

5.5 Water physical properties

The temperature of the water is a critical parameter needed to estimate the viscosity and density of the fluid. This behaviour can be observed in Fig. (11). The temperature of the water just after filling the tunnel was $T = 16.5°C$ and the final temperature $T = 23.5°C$. Therefore, the temperature used throughout the calculation of the Reynolds number was the average between them. Thus, the uncertainty of the temperature was the difference between the average and each sample. Once the temperature of the water was determined, its density and dynamic viscosity at such temperature were calculated using the equations from Section (3.5). The final values for each property are displayed in Table (5).

Property	Value	Uncertainty
Temperature, T $[°C]$	20.0	± 3.5
Density, ρ $[kg/m^3]$	998.20	± 0.72
Dynamic viscosity, μ $[kg/(m \cdot s)]$	$1.0022 \cdot 10^{-3}$	$(+0.0857, -0.0863) \cdot 10^{-3}$

Table 5: Water properties in the experiment.

As it can be observed in Table (5), the uncertainty in the dynamic viscosity is not symmetric (unlike the other properties). This is due to the fact that the $T = 20^oC$ laid right in the middle of the two different cases for the viscosity curve-fit, from Section (3.5). Therefore:

$$\left.\frac{d\mu}{dT}\right|_{T=20^oC^-} \neq \left.\frac{d\mu}{dT}\right|_{T=20^oC^+}$$

5.6 Flow visualization

Following the procedure described in Section (4.2), flow visualization was done at different angles of attack and free stream velocities in order to appreciate different flow regimes. The three different flow regimes described in Section (3.6) were found, and how the wake behaves after the cone was analyzed.

5.6.1 Laminar flow

Laminar flow is expected to occur at low local Reynolds Number, as explained in Section (3.6). To obtain a laminar flow regime, the free stream velocity inside the water tunnel was lowered to a very small value. Fig. (29) shows this laminar flow.

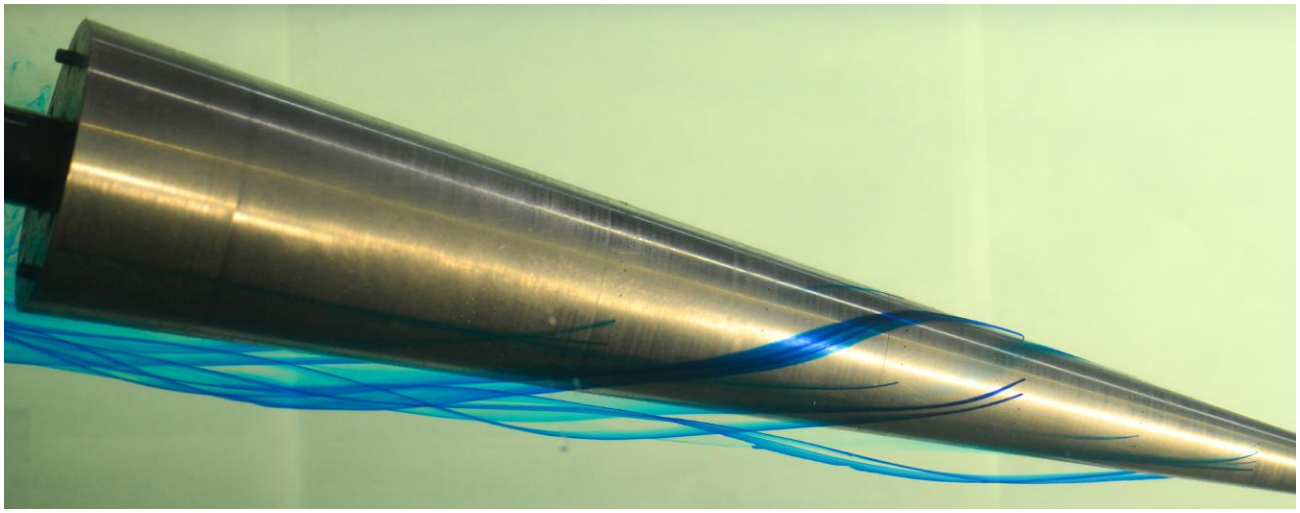

Figure 29: Laminar flow around the nosecone, at $\alpha = 15^o$.

α [^{o}]	$\Delta\alpha$ [^{o}]	U_∞ [m/s]	ΔU_∞ [m/s]	Re [$-$]	ΔRe [$-$]
15	± 0.1	0.0508	± 0.0084	$28.596 \cdot 10^3$	$(+5.333, -5.340) \cdot 10^3$

Table 6: Flow conditions in Fig. (29).

As it can be seen in Fig. (29), streamlines can be clearly identified. These streamlines never never cross each other or mix, so the flow regime is clearly laminar.

Also, it was identified that some vortices were developed underneath the cone. Fig. (30) shows the shape of these vortices, and Fig. (31) is a close up image of such vortices.

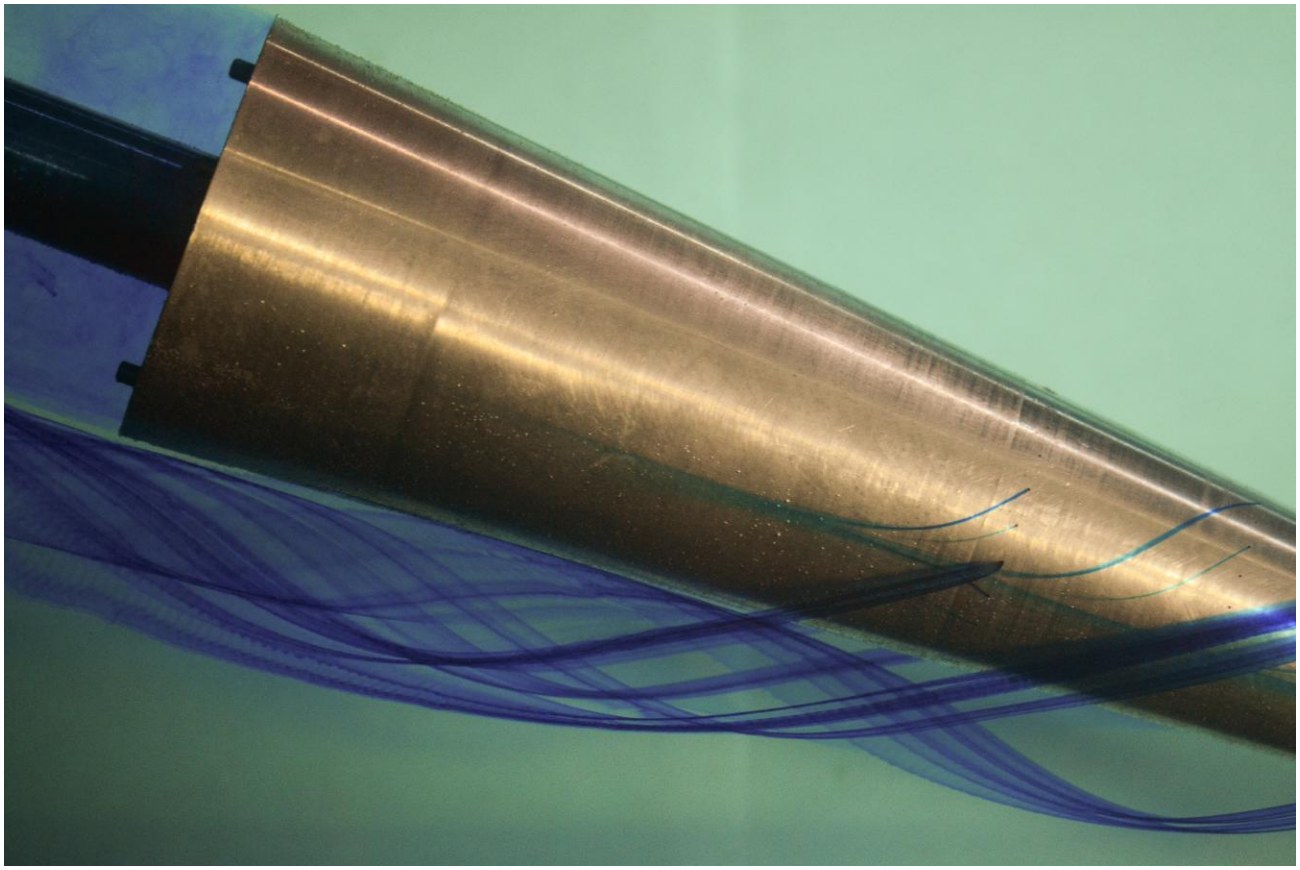

Figure 30: Laminar vortex around the nosecone, at $\alpha = 20^{o}$.

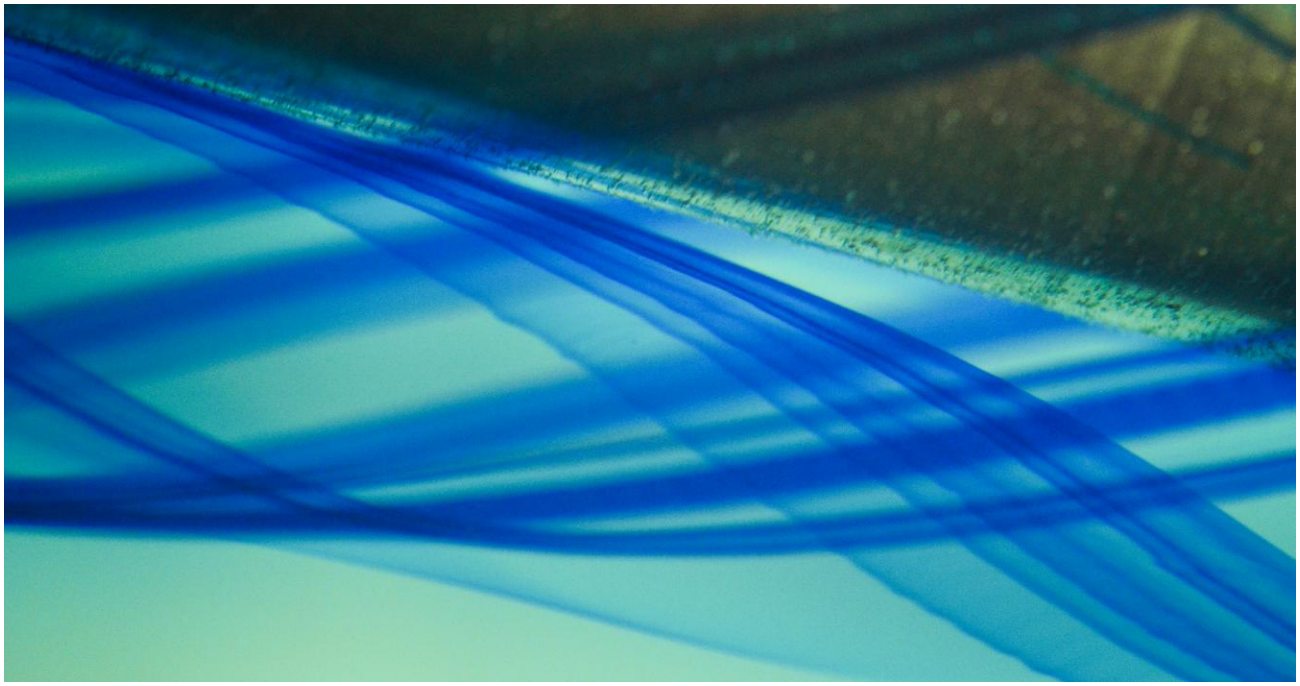

Figure 31: Closeup of laminar vortex around the nosecone, at $\alpha = 20^{o}$.

α [°]	$\Delta\alpha$ [°]	U_∞ $[m/s]$	ΔU_∞ $[m/s]$	Re $[-]$	ΔRe $[-]$
20	± 0.1	0.0508	± 0.0084	$28.596 \cdot 10^3$	$(+5.333, -5.340) \cdot 10^3$

Table 7: Flow conditions in Figs. (30) and (31).

As it can be observed in Figs. (30) and (31), the vortices are laminar, since the streamlines do not cross each other. The dye shows perfectly how the vortex is parallel to the cone, and the dye follows a helicoidal pattern. Furthermore these vortices were only found in the laminar flow regime, since in turbulent conditions the flow is chaotic and lacks any defined structure.

5.6.2 Turbulent flow

Turbulent flow is expected to occur at high local Reynolds number, as explained in Section (3.6). To obtain a turbulent flow regime, the free stream velocity inside the water tunnel was increased to a very high value. Figs. (32) and (33) show this turbulent flow, at increasing free stream velocities.

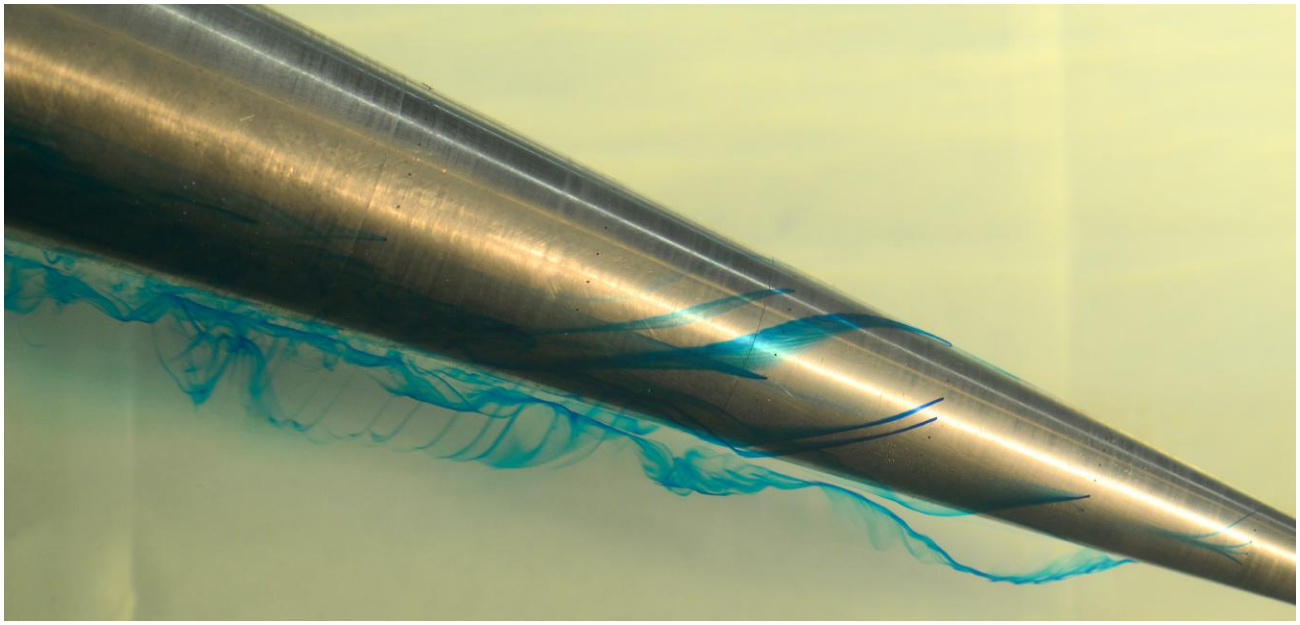

Figure 32: Turbulent flow around the nosecone, at $\alpha = 20^o$.

α [°]	$\Delta\alpha$ [°]	U_∞ $[m/s]$	ΔU_∞ $[m/s]$	Re $[-]$	ΔRe $[-]$
20	± 0.1	0.2286	± 0.0084	$128.68 \cdot 10^3$	$(+11.99, -12.05) \cdot 10^3$

Table 8: Flow conditions in Fig. (32).

As it can be observed in Fig. (32), the dye shows how the flow around the cone is completely turbulent and stochastic. However, the dye reveals that the boundary layer is attached to the cone, whereas in Fig. (33) the boundary layer is detached. Since in both cases the angle of attack is the same ($\alpha = 20^o$), the difference is given by the free stream velocity. In Fig. (33) the free stream velocity is higher, which causes the boundary layer separation to occur.

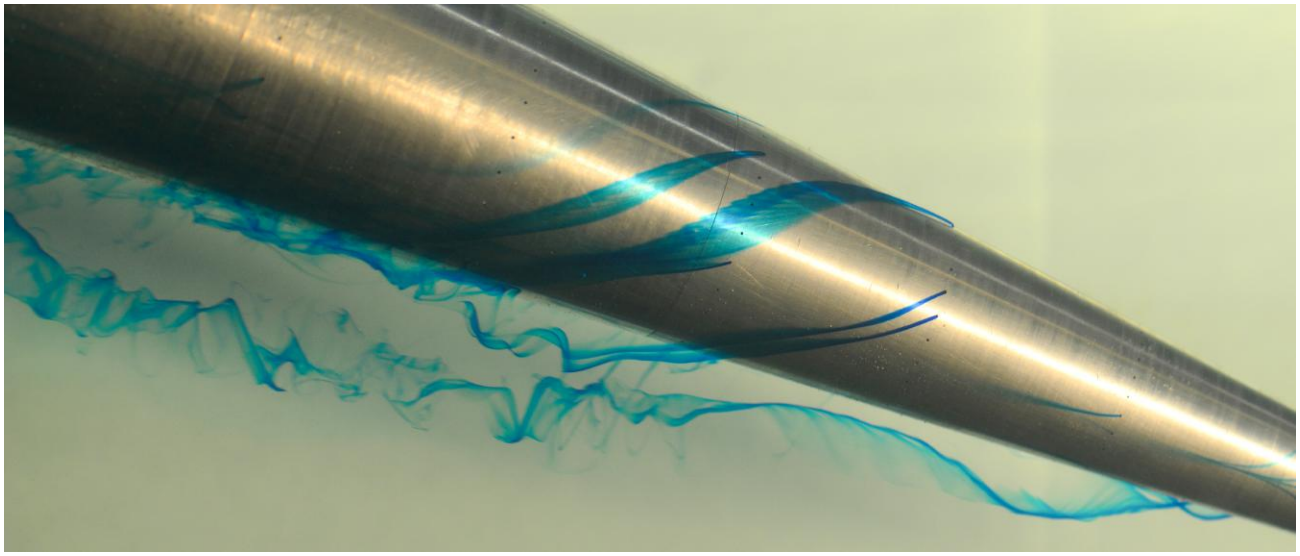

Figure 33: More turbulent flow around the nosecone with higher U_∞, also at $\alpha = 20^o$.

α [°]	$\Delta\alpha$ [°]	U_∞ $[m/s]$	ΔU_∞ $[m/s]$	Re $[-]$	ΔRe $[-]$
20	± 0.1	0.2794	± 0.0084	$157.28 \cdot 10^3$	$(+14.27, -14.35) \cdot 10^3$

Table 9: Flow conditions in Fig. (33).

5.6.3 Transitional flow

Transitional flow regime was expected to occur at a Reynolds number between the laminar and turbulent flow regimes, so the velocity had to be precisely adjusted to find just the correct Reynolds number range. Fig. (34) is a photograph where this transition was captured. As it can be observed, the transition from laminar to turbulent conditions occurred inside the red ellipse. At this point, the local Reynolds number increased from a value of laminar flow to a value of turbulent flow, so the transition took place.

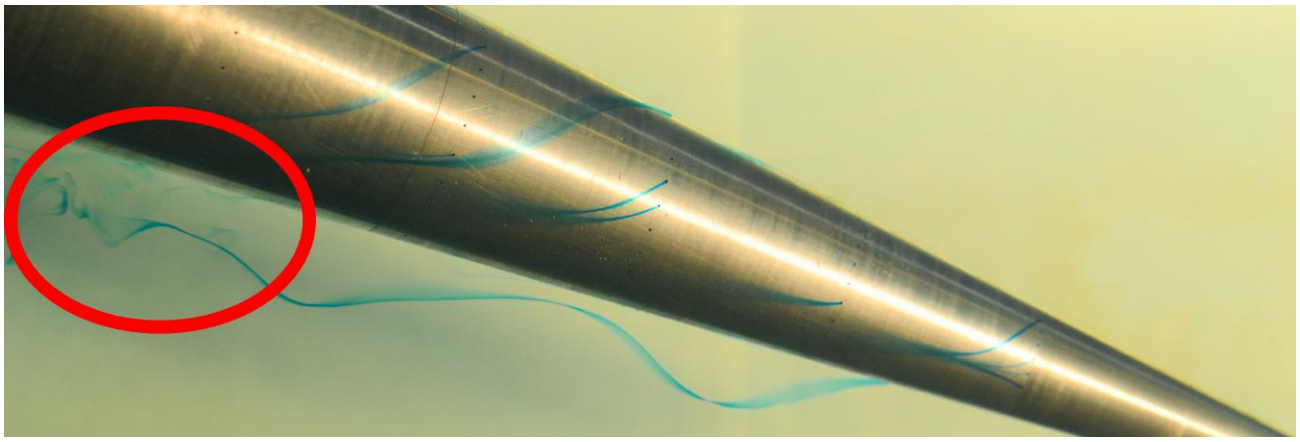

Figure 34: Transitional flow around the nosecone, at $\alpha = 20^o$.

α [°]	$\Delta\alpha$ [°]	U_∞ $[m/s]$	ΔU_∞ $[m/s]$	Re $[-]$	ΔRe $[-]$
20	± 0.1	0.1778	± 0.0084	$100.09 \cdot 10^3$	$(+9.79, -9.84) \cdot 10^3$

Table 10: Flow conditions in Fig. (34).

5.6.4 Wake

The wake of the cone was observed at different angles of attack and free stream velocities. It was found that in every case a recirculation region was formed, but the dye would rapidly dissipate into the water and difficulted the observation.

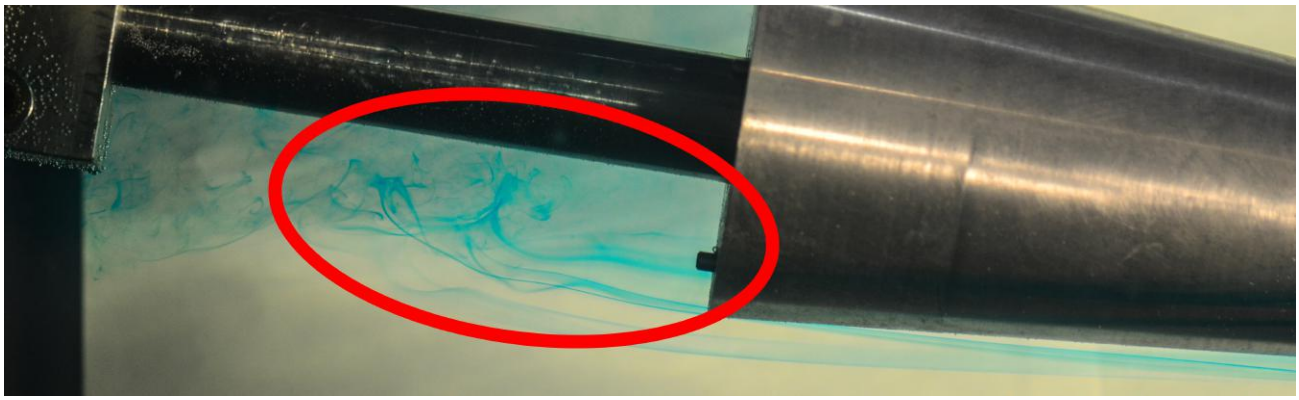

Figure 35: Flow at the wake of the nosecone, at $\alpha = 10^{o}$.

α [°]	$\Delta\alpha$ [°]	U_∞ $[m/s]$	ΔU_∞ $[m/s]$	Re [–]	ΔRe [–]
10	± 0.1	0.1270	± 0.0084	$71.490 \cdot 10^3$	$(+7.737, -7.769) \cdot 10^3$

Table 11: Flow conditions in Fig. (35).

As it can be observed in Fig. (35), the dye would deviate towards the middle of the cone after flowing past its trailing edge. This shows that there was a recirculation region of lower flow velocity and higher vorticity.

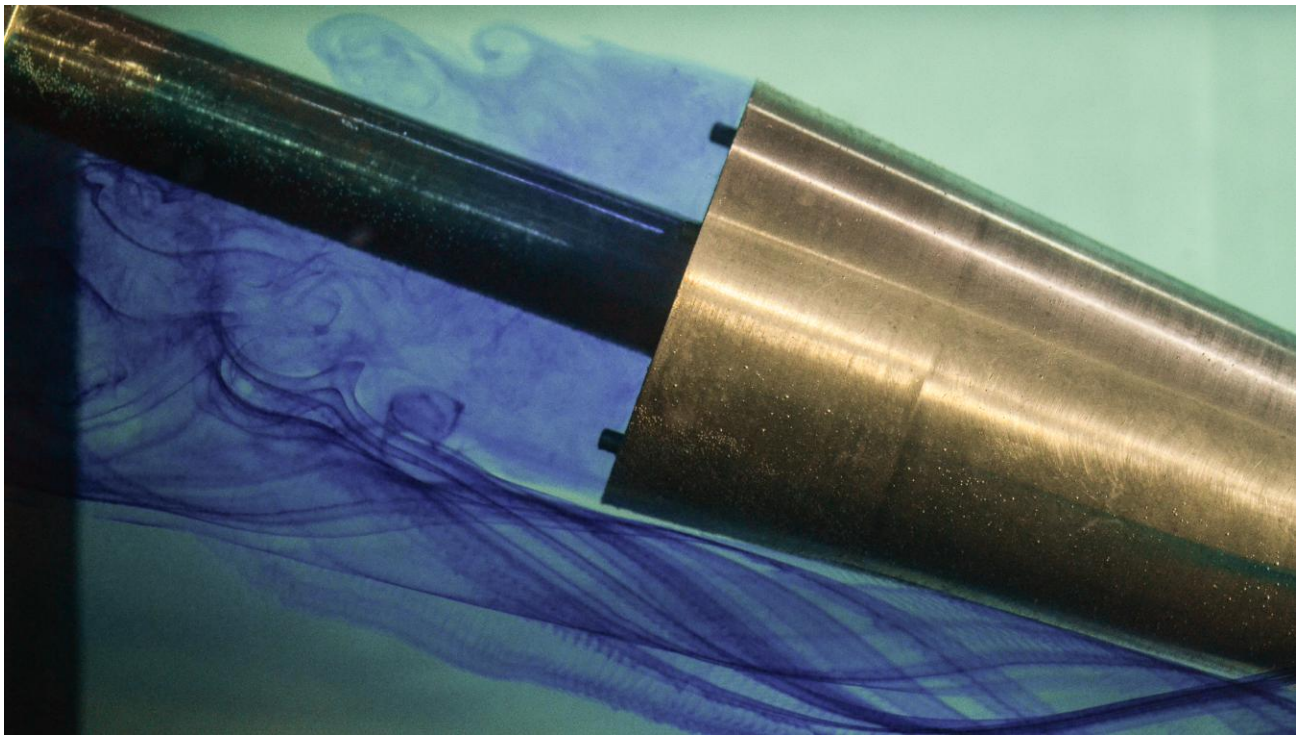

Figure 36: Flow at the wake of the nosecone, at $\alpha = 20^{o}$.

α [°]	$\Delta\alpha$ [°]	U_∞ $[m/s]$	ΔU_∞ $[m/s]$	Re $[-]$	ΔRe $[-]$
20	± 0.1	0.1016	± 0.0084	$57.192 \cdot 10^3$	$(+6.812, -6.835) \cdot 10^3$

Table 12: Flow conditions in Fig. (36).

As it can be observed in Fig. (36), dye was concentrated in the wake of the cylinder. As it can be observed in the top of the image, some eddies can be appreciated, which were a result of the very high vorticity of this region. Furthermore, in this figure the laminar vortices can clearly be observed due to the high amount of dye injected.

5.6.5 Jets

In order to purge the holes in the cone, water was ejected from the holes when the free stream velocity was zero. However when doing that, the remaining dye that was on the lines was rapidly ejected creating jets. This behaviour is displayed in Fig. (37).

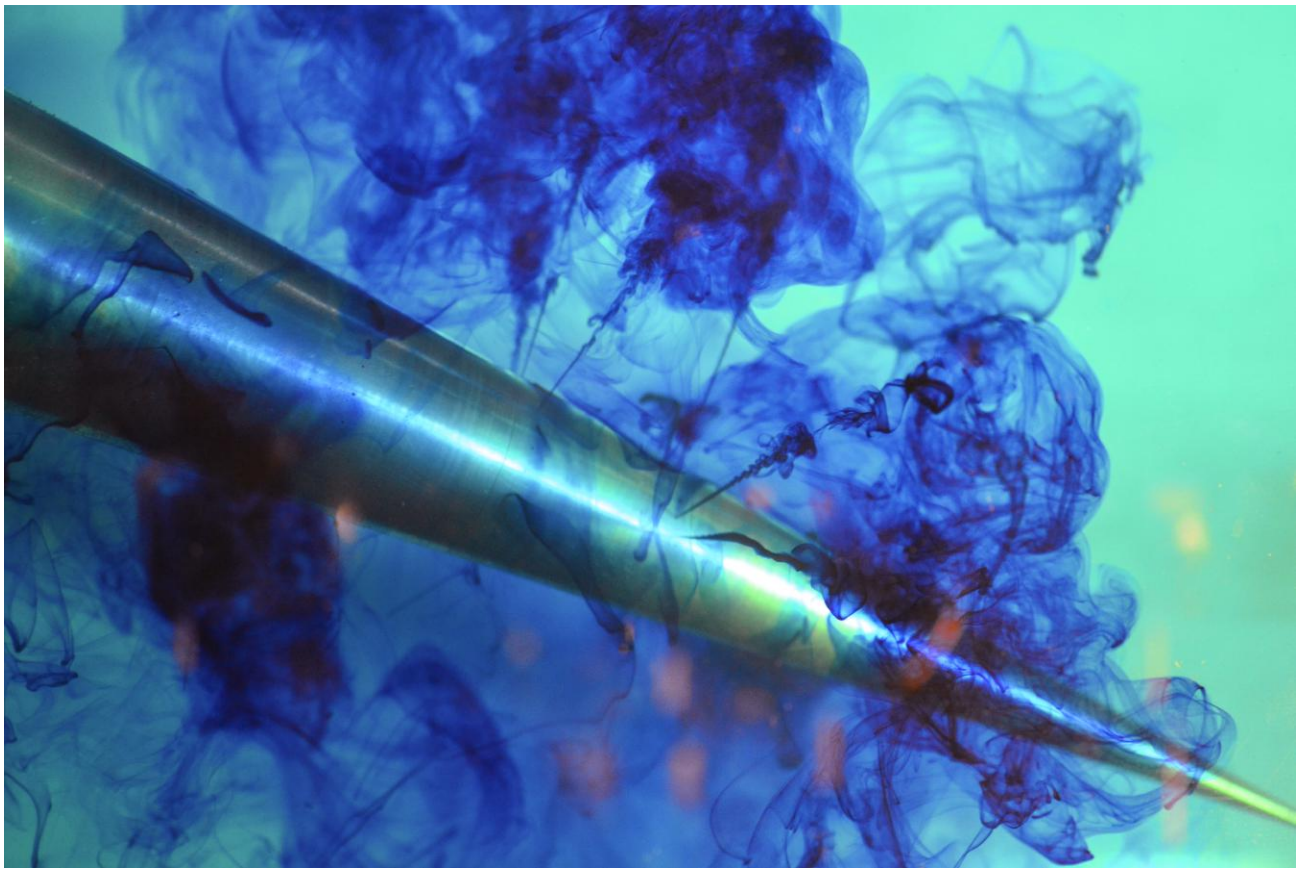

Figure 37: Jets around the nosecone, at $\alpha = 20^o$ and $U_\infty = 0$.

Although this was not the original scope of the experiment, a photograph was taken because it can be seen how the jets transitioned from laminar to turbulent conditions at some point along the jet.

5.7 Boundary layer

The last phenomenon to be analyzed was to measure the boundary layer profile. In order to do so, LDV data points were taken vertically along the vertical plane of symmetry of the cone. However, the boundary layer could not

be observed. A possible reason why this happened is because at the measurement point, the boundary layer thickness was of the order of the probe volume. The probe volume is the region where the two beams intersect, and the particles cross to measure their velocity. Thus, if this volume is as large as the boundary layer thickness, the velocity deficit caused by the boundary layer is not possible to be observed.

5.8 Sources of error

Some of the most important sources of error that may have had a principal role during the data acquisition processes were:

- Excessive noise in the LDV signal output: For every LDV measurement there were two different dominant frequencies, and it was thought that one of this frequencies was caused by noise in the signal. This may be due to a slight LDV missalignment, or by some malfunctioning of the high-pass filter. This was the reason why Δf had such a high value.
- Pump power fluctuations: It was found that the speed of the water tunnel was not steady. It randomly changed in the range of $\pm 0.1\ in/s$, despite the power of the pump being kept constant.
- Real flow effects: Some ideal assumptions were introduced to analyze the complex flow inside the tunnel, such as assuming that the water tunnel components were perfectly isentropic. This assumption is not completely true in the real world, since some entropy is inevitably always generated. The free stream flow was assumed to reach the test object unperturbed and with a uniform velocity, also ignoring three-dimensional and boundary layer effects. Although such a perfect flow can never be achieved inside a water tunnel, it was considered that these real effects were weak enough to be neglected.
- Surface waves: Waves were formed on the surface of the water tunnel. It was observed that these waves were stronger at faster free stream velocities. They were not considered to change significantly the flow conditions, as long as the test region was submerged deep enough from the surface of the water.

5.9 Future progress

Some other experiments that could have been conducted if more time had been available are the following:

- Increase the angle θ accuracy: By increasing the accuracy in the measurement of θ it would be possible to calculate the flow velocity more precisely. This could be done by projecting the angle to a wall further away, and measuring the distances with a more precise method.
- Try to reduce the noise in the LDV signal: As previously explained, one of the greatest sources of error when measuring the velocity using LDV is the noise of the signal. Two peaks in amplitude were found for most cases and it was unclear which was the dominant frequency. This problem might be solved if another high pass filter was used or if the alignment of the LDV was revised.
- Increase the sampling frequency: A higher sampling frequency would imply a higher resolution in the frequency reading obtained from the LDV. This would allow to increase the accuracy of the velocity calculations and be able to notice small changes in velocity. Being able to observe this small velocity changes would allow to obtain a more precise velocity distribution, which would help when trying to model this phenomenon.
- Consider other probability distribution functions: In Section (5.3), it was concluded that a normal distribution was able to model the velocity distribution of the particles in the flow with a reasonable degree of accuracy. However, other probability distribution function might had better correlate the real velocity distribution. Therefore,

more time could be spent trying to find a probability distribution function that better matched the experimental results.

- Velocity field around the cone: Getting velocity readings as the fluid moves around the cone would allow to get a better idea of the velocity field around the cone. This result could be latter compared with the velocity field predicted by the potential flow theory or CFD.

Other experiments that could be interesting to perform if more instruments and resources were available are:

- Use a laser with a smaller probe volume to measure the boundary layer: As previously explained, it was not possible to measure the boundary layer of the cone. Using a LDV with a smaller probe volume would have helped to measure the boundary layer thickness.
- Study other test objects: Other test objects such as airfoils or even model airplanes could be measured. Taking advantage of the fact that a high Reynolds number can be achieved in the water tunnel could allow to reproduce the Reynolds number that the full scale aircraft would face.
- Velocity measurements inside the wake: It would be interesting to study the flow field inside the wake of the cone. As the wake of the cone was typically turbulent, it was difficult to study it experimentally and extremely challenging to model. Therefore, more experimental analysis could be done in order to have a better understanding of it.

6 Conclusions

This experimental session was divided into two different sets of experiments: LDV measurements and flow visualization, with different objectives each.

LDV was used to perform velocity measurements in the flow. The basic physics behind laser Doppler velocimetry were studied and used to obtain precise measurements with it. This task became challenging due to different sources of error, such as the low precision of the angle between the two laser beams. This fact downgraded the quality of the results, however it was possible to obtain accurate enough results for our purposes. The high pass filter, used in the signal processing and data acquisition process often overloaded invalidating the results obtained while it was overloaded. Moreover, identifying the dominant frequency turned out to be a difficult task due to excessive noise in the signal.

After learning how to obtain velocity readings from the LDV in a proficient manner, differences between flowmeter and LDV velocities were studied. It was found that LDV and flowmeter values of the velocity were very similar. Thus, it was considered that the velocity reading given by the flowmeter was accurate enough for practical purposes.

A statistical analysis of the velocity distribution of the flow field in the free stream was performed. In order to do so, two probability distribution functions were considered: Weibull and normal distribution functions. For both of them, the mean and variance of experimental data were used as input. Then, the probability of finding a particle within a certain velocity range was compared for both analytic velocity distribution functions and the actual experimental distribution. By doing so, it was determined that the best model for the velocity distribution in the free stream was the normal distribution.

Also, the root mean square velocity and turbulence of the free stream were studied. For both analytic models the root mean square of the velocity fluctuations was found to be equal to the standard deviation. Experimental and

theoretical results almost correlate perfectly when calculating U_{rms}. Appart from that, it was performed a curve fit for U_{rms} and U_{rms}/U_∞ versus U_∞ to analyze the trend of these parameters as a function of the free stream velocity. This lead to a surprising and interesting result which is that there is a given value of U_∞ that minimizes the amount of turbulence of the flow.

Water properties are highly dependent on the temperature. As there was a high uncertainty on that temperature, density and dynamic viscosity could not be precisely determined. That is why the uncertainty in the Reynolds number turned out to be so large.

From the flow visualization perspective, the flow around a cone was studied at different velocities and angles of attack. The most noticeable features of the flow at low velocities were a pair of laminar vortices. For higher velocities, the local Reynolds number increased and it was possible to observe the transition from laminar to turbulent flow conditions. Also, when setting the tunnel to even higher speeds, fully turbulent flow was observed. Furthermore, boundary layer separation was observed for very high free stream velocities.

Finally, the boundary layer profile was tried to be measured. However, It was not possible to obtain any relevant results, mainly due to the fact that the LDV used had a large probe volume. Thus it was not suited to measure such a small region as the boundary layer.

7 References

[1] Dryden Flight Research Center ECN 33298-036 (Photographed 1985).

[2] Lincoln P. Erm and Michael V. OL "*An Assessment of the Usefulness of Water Tunnels for Aerodynamic Investigations*", Air Vehicles Division Defence Science and Technology Organisation, United States Air Force Research Laboratory, (DSTO-TR-2803) www.dtic.mil/get-tr-doc/pdf?AD=ADA582450

[3] Sullivan J. "*Notes on Laser Doppler Velocimetry*", AAE 520 Experimental Aerodynamics (2004).

[4] Anderson, John D. Jr. "*Fundamental of Aerodynamics*", (5th ed.).

[5] Casella G. and Berger Roger L. "*Statistical Inference*", (2nd ed.), Duxbury, (2001).

[6] Fréchet, M. "*Sur la loi de probabilité de l'écart maximum*", Annales de la Société Polonaise de Mathematique, Cracovie, (1927).

[7] Davis, Philip J. "*Leonhard Euler's Integral: An Historical Profile of the Gamma Function*", American Mathematical Monthly, vol. 66 (1959).

[8] Crittenden, J.; Trussell, R.; Hand, D.; Howe, K. and Tchobanoglous, G. "*Water Treatment: Principles and Design*", Appendix C, (3rd ed.).

[9] Heiser, William H. and Pratt, David T. "*Hypersonic Airbreathing Propulsion*", AIAA Education Series, (1994).